14. GEOCHEMISTRY OF THE DURICRUST DEPOSITS

It was observed that carnotite and calcite are intimately associated in the calcrete. The question now arises: what were the controlling factors, from the geochemical standpoint, that resulted in the precipitation of these minerals and all the associated epigenetic major and trace elements? This chapter therefore deals with the factors which influenced the dissolution, transportation and precipitation of elements in duricrust deposits.

14.1 Analytical Results

Most of the analytical work for this section was done on samples of calcrete powder obtained from boreholes of percussion drilling at the Langer Heinrich. Tables 26 and 27 are the results of partial whole-rock analyses of the powdered calcrete. Atomic absorption was used for the analyses in Table 26. In Table 27 the following analytical methods were used: uranium - delayed neutron counting; carbon dioxide (for $CaCO_3$) - Leco gas absorption; and sulphate-photometry. Partial whole-rock chemical analysis for the hardpan of the Langer Heinrich formation is given in Table 28. Analysis was by atomic absorption and delayed neutron counting.

Semi-quantitative spectrographic analysis for trace elements in the calcrete powder is given in Table 29.

Partial chemical analyses of the epigenetic fractions of calcrete powders are given in Table 30. The calcrete was

leached with dilute hydrochloric acid from which the detrital residue was filtered off. The filtrate was evaporated to dryness and it was upon this dried portion that the analyses were performed. All calculations were therefore based on the weight of sample taken from the dried acid soluble fraction and not on the weight of the whole rock. The value for the detritus was nearly the difference in weight between the whole-rock sample initially used and the residue after leaching and filtration.

The major elements including barium and strontium were analyzed by conventional flame atomic absorption, lead and vanadium by atomic absorption using the carbon rod technique, and uranium by delayed neutron counting. The remaining trace elements were determined by non-destructive neutron activation analysis.

TABLE 26: PARTIAL WHOLE-ROCK CHEMICAL ANALYSES OF CALCRETE POWDERS FROM PERCUSSION BOREHOLES AT THE LANGER HEINRICH

	Borehole HJ2						Borehole J1						Borehole HJ1				Borehole C5																Borehole AD1													
%	HJ2-6 (3)*	HJ2-8 (4)	HJ2-10 (5)	HJ2-13 (6,5)	HJ2-15 (7,5)	HJ2-18 (9)	J1-4 (2)	J1-6 (3)	J1-10 (5)	J1-11 (5,5)	J1-12 (6)	J1-14 (7)	HJ1-1 (0,5)	HJ1-2 (1)	HJ1-3 (1,5)	HJ1-4 (2)	C5-5 (2,5)	C5-10 (5)	C5-12 (6)	C5-13 (6,5)	C5-14 (7)	C5-15 (7,5)	C5-18 (9)	C5-24 (12)	C5-26 (13)	C5-28 (14)	C5-36 (18)	AD1-8 (4)	AD1-12 (6)	AD1-16 (8)	AD1-17 (8,5)	AD1-19 (9,5)	AD1-20 (10)	AD1-25 (12,5)	AD1-28 (14)	AD1-29 (14,5)	AD1-30 (15)	AD1-31 (15,5)	AD1-32 (16)	AD1-48 (24)
SiO_2	40,8	55,0	58,3	64,3	44,4	65,7	64,8	63,0	58,6	60,4	50,5	60,0	43,7	53,8	60,4	51,2	42,5	50,8	54,0	54,3	58,4	51,5	49,8	58,2	59,2	59,3	56,4	59,1	70,1	55,7	52,1	46,9	52,2	60,8	68,1	60,4	45,3	47,1	54,3	68,4
TiO_2	0,14	0,14	0,18	0,18	0,12	0,21	0,24	0,22	0,26	0,19	0,21	0,30	0,13	0,14	0,12	0,39	0,23	0,17	0,23	0,31	0,39	0,48	0,20	0,12	0,45	0,33	0,17	0,14	0,20	0,14	0,12	0,13	0,10	0,22	0,13	0,11	0,12	0,11	0,30	0,27
Al_2O_3	7,60	9,63	9,89	10,60	8,17	10,92	8,20	9,52	9,88	9,08	9,07	11,07	5,54	8,01	8,99	10,60	7,56	8,13	7,94	7,83	9,54	10,79	7,85	9,11	9,46	9,09	8,98	8,87	10,46	8,50	7,70	7,35	7,73	10,10	10,84	9,17	7,45	7,73	8,95	11,50
Fe_2O_3	1,33	1,38	1,77	1,87	1,35	2,17	2,07	1,78	2,46	2,01	1,99	2,96	0,92	0,95	0,86	4,28	1,40	1,26	1,63	2,01	2,62	3,38	1,29	0,97	3,28	2,70	1,45	1,26	1,98	1,37	1,31	1,32	1,04	2,13	1,34	1,24	1,17	1,21	2,36	2,87
MnO	0,02	0,02	0,04	0,04	0,02	0,05	0,04	0,05	0,06	0,07	0,04	0,11	0,02	0,03	0,03	0,05	0,02	0,03	0,04	0,03	0,4	0,04	0,02	0,02	0,08	0,07	0,02	0,03	0,07	0,03	0,02	0,03	0,03	0,09	0,03	0,03	0,03	0,03	0,19	0,29
MgO	0,81	0,75	0,90	0,89	0,73	0,91	0,99	2,05	2,82	1,02	1,04	2,46	2,56	1,20	0,85	2,65	0,90	0,80	0,79	1,21	1,63	2,14	1,01	0,82	1,77	1,37	1,00	3,45	3,42	2,24	2,11	1,95	1,26	1,46	1,16	1,09	1,20	0,88	1,38	1,32
CaO	24,7	13,82	12,48	7,40	23,06	5,55	8,12	9,33	10,07	9,95	15,19	6,23	18,86	14,89	12,03	12,76	21,58	15,83	13,55	13,16	9,60	11,93	17,26	12,21	10,56	10,18	14,00	9,39	2,37	11,45	15,05	19,63	16,68	8,50	2,39	9,63	20,16	19,10	12,60	2,30
Na_2O	1,46	1,50	1,83	1,34	1,48	1,60	1,64	1,52	1,90	1,64	1,77	1,86	2,0	2,41	2,44	2,20	1,74	1,94	1,66	1,57	1,87	1,82	1,54	1,98	1,28	1,44	1,71	1,81	1,89	1,56	1,43	1,29	1,44	1,85	2,20	1,68	1,28	1,41	1,39	1,77
K_2O	2,23	3,24	3,00	1,40	2,64	3,61	3,05	2,77	3,02	2,76	2,99	3,64	1,92	2,95	3,40	3,14	1,95	2,40	2,63	2,23	2,50	2,69	2,26	2,84	1,78	2,50	2,75	3,16	3,98	3,21	2,81	2,69	2,84	3,65	3,85	3,40	2,39	2,65	2,81	4,02
P_2O_5	0,08	0,11	0,13	0,14	0,12	0,19	0,13	0,12	0,14	0,10	0,14	0,18	0,09	0,12	0,10	0,11	0,07	0,08	0,08	0,06	0,07	0,07	0,08	0,08	0,17	0,15	0,10	0,14	0,18	0,11	0,11	0,10	0,11	0,16	0,13	0,12	0,10	0,10	0,15	0,27
ppm																																									
Li	29	33	39	39	24	35	18	27	44	29	28	30	101	37	34	62	17	16	18	22	29	38	17	18	41	34	18	258	342	181	158	128	105	145	124	114	64	50	124	86
U	1 250	1 907	530	937	413	190	93	71	230	936	675	65	122	63	36	40	73	366	641	405	590	869	519	354	362	70	291	53	178	79	1 158	221	264	10	73	220	742	62	123	67

* The figure in brackets refers to the depth in metres.

CONFIDENTIAL

TABLE 27: URANIUM, CARBONATE AND SULPHATE ANALYSES OF CALCRETE POWDERS FROM PERCUSSION BOREHOLES AT THE LANGER HEINRICH

Depth (m)	Borehole HJ1			Borehole HJ2			Borehole J1			Borehole C5			Borehole AD1		
	U(ppm)	$CaCO_3$ (%)*	SO_4 (%)	U(ppm)	$CaCO_3$ (%)	SO_4 (%)	U(ppm)	$CaCO_3$ (%)	SO_4 (%)	U(ppm)	$CaCO_3$ (%)	SO_4 (%)	U(ppm)	$CaCO_3$ (%)	SO_4 (%)
0,5 (1)+	122	21,8	12,2	2	1,2	0,01	13	12,4	0,01	-	-	-	120	6,8	2,8
1,0 (2)	63	25,5	1,76	-	-	-	34	11,6	0,01	335	30,9	0,14	-	-	-
1,5 (3)	36	20,5	0,74	16	9,4	0,01	49	11,7	0,01	-	-	-	-	-	-
2,0 (4)	40	20,2	0,38	30	17,8	0,01	93	10,6	0,01	-	-	-	37	1,4	0,02
2,5 (5)	19	43,8	0,14	21	28,8	0,01	74	11,3	0,01	73	40,2	0,04	-	-	-
3,0 (6)	-	-	-	1 250	40,7	0,03	74	13,1	0,01	-	-	-	-	-	-
3,5 (7)	-	-	-	-	-	-	163	13,5	0,34	-	-	-	-	-	-
4,0 (8)	13	48,2	0,19	1 890	24,1	0,01	244	10,4	0,23	-	-	-	53	19,8	0,02
4,5 (9)	-	-	-	-	-	-	105	6,5	0,48	-	-	-	-	-	-
5,0 (10)	-	-	-	530	22,6	0,01	230	15,6	0,02	366	31,9	0,03	-	-	-
5,5 (11)	-	-	-	52	12,9	0,24	944	17,9	0,01	434	36,5	0,02	-	-	-
6,0 (12)	15	46,1	1,26	-	-	-	675	26,4	0,01	641	27,2	0,02	178	2,9	0,02
6,5 (13)	-	-	-	935	12,9	0,02	260	11,4	0,02	405	25,6	0,02	-	-	-
7,0 (14)	-	-	-	757	12,9	0,01	65	9,1	0,01	587	18,6	0,01	-	-	-
7,5 (15)	-	-	-	413	41,6	0,02	25	2,1	0,02	870	19,8	0,03	47	16,1	0,01
8,0 (16)	8	45,3	0,04	-	-	-	SCHIST CONTACT			460	25,3	0,03	80	24,0	0,01
8,5 (17)	-	-	-	-	-	-				-	-	-	1 158	30,1	0,01
9,0 (18)	-	-	-	1 142	9,2	0,01				520	33,0	0,02	200	33,9	0,02
9,5 (19)	-	-	-	GRANITE CONTACT						-	-	-	220	36,2	0,01
10,0 (20)	2	39,4	0,01							-	-	-	264	29,9	0,02
10,5 (21)	-	-	-							-	-	-	114	26,7	0,02
11,0 (22)	-	-	-							-	-	-	70	22,5	0,03
11,5 (23)	-	-	-							-	-	-	-	-	-
12,0 (24)	46	38,0	0,02							354	23,8	0,01	-	-	-
12,5 (25)	-	-	-							-	-	-	10	14,1	0,02
13,0 (26)	-	-	-							382	20,2	0,01	-	-	-
13,5 (27)	-	-	-							-	-	-	-	-	-
14,0 (28)	142	37,6	0,01							70	18,5	0,01	73	3,1	0,01
14,5 (29)	-	-	-							-	-	-	220	15,5	0,02
15,0 (30)	-	-	-							-	-	-	740	35,2	0,03
15,5 (31)	-	-	-							-	-	-	62	34,1	0,24
16,0 (32)	30	26,1	0,01							442	17,0	0,01	123	21,2	0,02
16,5 (33)										-	-	-	-	-	-
17,0 (34)										-	-	-	-	-	-
17,5 (35)										-	-	-	-	-	-
18,0 (36)										290	25,3	0,03	18	15,6	0,01
18,5 (37)													-	-	-
19,0 (38)													-	-	-
19,5 (39)													-	-	-
20,0 (40)													42	14,5	0,02
20,5 (41)													-	-	-
21,0 (42)													-	-	-
21,5 (43)													-	-	-
22,0 (44)													20	19,8	0,02
22,5 (45)													-	-	-
23,0 (46)													-	-	-
23,5 (47)													-	-	-
24,0 (48)													67	2,3	0,02
24,5 (49)													-	-	-
25,0 (50)													-	-	-
25,5 (51)													-	-	-
26,0 (52)													48	15,6	0,02
26,5 (53)													-	-	-
27,0 (54)													-	-	-
27,5 (55)													-	-	-
28,0 (56)													40	10,9	0,02
28,5 (57)													-	-	-
29,0 (58)													-	-	-
29,5 (59)													42	8,9	0,02

* $CaCO_3$ content calculated from CO_2 values.

\+ Number in brackets refers to the sample number, i.e. 0,5 (1) for borehole HJ1 means sample HJ1-1 from a depth of 0,5 m.

CONFIDENTIAL

TABLE 28: PARTIAL WHOLE-ROCK CHEMICAL ANALYSES OF THE HARDPAN CALCRETE OF THE LANGER HEINRICH CALCRETE FORMATION

%	LH 7	LH 24
SiO_2	32,9	32,6
TiO_2	0,15	0,16
Al_2O_3	4,74	5,27
Fe_2O_3	0,94	0,81
MnO	0,02	0,02
MgO	0,84	1,46
CaO	29,86	31,3
Na_2O	0,91	1,04
K_2O	2,18	1,84
P_2O_5	0,11	0,09
ppm		
Li	7	10
U	-	481

LH 7: Sample taken from the main body of hardpan overlying the Bloedkoppie Granite.

LH 24: Hardpan of the boulder calcrete type located on the Bloedkoppie Flats - contains carnotite.

TABLE 29: SEMI-QUANTITATIVE SPECTROGRAPHIC ANALYSES FOR TRACE ELEMENTS IN THE CALCRETE POWDERS FROM PERCUSSION BOREHOLES AT THE LANGER HEINRICH (COURTESY, ANGLO AMERICAN RESEARCH LABORATORIES)

SAMPLE NUMBER		PARTS PER MILLION														
		Bi	Pb	Zn	Sb	Sn	Y	Be	Mo	Nb	Cu	Ni	La	Ag	Co	V
C-5	5	<1,0	15	<10	<50	<5	<10	<0,1	<5	<100	60	15	<100	<0,1	<10	80
	10		40	10		5	15				15	15		0,2		200
	13		20	10		<5	100				10	20		<0,1	10	250
	14		15	<10			20				8	25			<10	300
	15		15				20				10	20				400
	16		10				<10				20	15				150
	18		25	10			10				15	10		0,1		200
	26		10	<10			30				30	40		<0,1	15	200
	28		10	<10			30				25	40		<0,1	10	200
	36		30	10			15				30	25		0,1	25	200
HJ-1	1		<10	<10			<10				15	<10		0,6	<10	150
	2		20								8			<0,1		80
	3		25								5					70
	4		20	10		5	25	0,1			30	30			15	100
	5		30	<10		5	15	<0,1			25	25			<10	300
HJ-2	6		20	15		<5	<10				20	30			15	300
	8		25								15	25			10	500
	10	5	20				50	0,1			25	25			10	300
	13	<1,0	30			5	10	<0,1			25	20			10	400
	15		20	10		<5	<10				10	<10		0,1	<10	100
	18		20				10				25	25				150
J-1	2		10			<5	10	<0,1			25	15				200
	4		15			<5	15	<0,1			25	20				80
	6		25	10		5	60	0,1			20	30			15	150
	8		10	<10		<5	15	0,8			15	15			<10	200
	10		25			8	20	<0,1	5		30	60			10	150
	12		15			<5	15		<5		25	40			15	200
	14		10				15				20	25			10	100
AD-1	8		20	10			<10				15	<10			<10	100
	12		15	<10			15				20	40				200
	16		15	15			20	1,5			15	10				100
	17		30	25			15	<0,1			25	40			20	600
	18		20	<10			<10				15	15			<10	100
	19		10	15			20				20	10				150
	20		25	<10			<10				10	<10				100
	25		15				15	<0,1			20	20				100
	28		25				<10				15	10				70
	29		25			5	10				20	15				200
	30		10	15		<5	20				20	10			10	250
	31		40	10		<5	10				20	20			<10	100
	32		30	10		5	25	0,1			25	60			30	200
	48	1	25	<10		5	30	<0,1	1		40	25			20	150

TABLE 30: PARTIAL CHEMICAL ANALYSES OF THE EPIGENETIC FRACTION OF CALCRETE POWDERS FROM PERCUSSION BOREHOLES AT THE LANGER HEINRICH

%	1	2	3	4	5	6	7	8	9	10	11	12	13
	HJ2-3	HJ2-5	HJ2-10	HJ2-13	HJ2-15	AD1-8	AD1-17	AD1-25	AD1-30	J1-6	J1-11	C5-15	C5-24
SiO_2	4,3	2,9	2,8	1,9	1,1	1,8	1,3	0,5	0,8	1,4	1,1	1,3	0,8
Al_2O_3	5,8	1,3	2,6	4,0	1,5	2,6	1,8	5,4	1,6	4,0	2,6	4,6	2,8
Fe_2O_3	6,6	1,5	1,9	2,9	1,1	2,3	1,5	3,3	1,3	4,5	2,9	3,5	2,3
MgO	2,1	0,7	0,9	1,2	0,6	10,5	3,6	4,8	1,6	1,6	1,1	1,8	0,5
CaO	40,7	47,4	44,4	42,1	47,4	44,5	44,8	43,5	46,5	44,1	47,9	44,5	46,7
Na_2O	0,6	0,5	0,8	1,2	0,3	1,3	0,5	1,0	0,3	0,7	0,8	0,5	0,3
K_2O	2,2	0,7	1,4	1,9	0,6	1,2	0,9	2,4	0,8	1,1	1,1	2,0	1,2
Detritus	87,8	70,2	77,4	85,9	59,6	77,8	69,3	83,8	63,7	84,2	80,5	77,0	75,9
ppm													
Ba	249	47	116	217	51	117	47	902	82	311	511	113	51
Ce	72	18	20	37	17	21	9	47	13	34	37	34	16
Co	21	9	8	13	3	9	5	25	3	19	23	8	5
Dy	3	1	2	4	1	1	1	1	1	1	3	2	1
Eu	1,2	0,4	0,6	1,0	0,3	0,5	0,2	0,9	0,3	0,5	0,6	0,8	0,3
La	51	12	15	20	18	13	9	32	7	21	25	23	8
Lu	0,3	0,1	0,2	0,2	0,05	0,1	0,03	0,2	0,2	0,1	0,2	0,2	0,1
Pb	8	7	15	22	4	8	5	22	6	6	9	9	6
Sc	6	3,3	2,8	4,6	1,4	2,2	2,0	3,3	0,8	1,5	1,6	1,7	1,2
Sm	12	3	4	7	2	2	2	8	2	5	6	8	3
Sr	180	9	111	206	166	164	25	110	194	419	281	148	177
U	83	53	1 412	3 904	385	123	2 375	44	1 332	85	2 527	2 571	1 043
V	147	55	297	896	138	96	458	190	276	130	610	580	230
Yb	2,2	0,8	1,6	2,0	0,8	0,7	0,3	1,3	0,4	1,1	1,1	1,5	0,5
Ratio													
U/V	0,56	0,96	4,75	4,36	2,97	1,28	5,19	0,23	4,83	0,65	4,14	4,43	4,53

Note:

(1) The results of the analyses are calculated on the basis of $CaCO_3$ only and not on the whole rock. (See text).

(2) The depth of the borehole in metres is obtained by dividing the last figure of the sample number by 2.

CONFIDENTIAL

14.2 General Chemistry of the Calcretes

This section deals briefly with the general chemistry of the calcrete of the Langer Heinrich as represented by powders from the percussion boreholes (Tables 26 and 27) and the analysis of the hardpan (Table 28).

Perusal of the data of Table 26 reveals that the main constituents are silica, alumina and calcium oxide. The first two form part of the detrital fraction, and calcium oxide the cement. Of the minor constituents, the oxides of potassium, sodium, iron and magnesium form the next most abundant group of elements. Minor amounts of oxides of titanium, manganese and phosphorus were found. The only trace elements determined were lithium and uranium.

Comparing these results with the world average values (Table 31) as given by Goudie (1972) it is evident that the calcretes of the Langer Heinrich are dissimilar.

It would seem that Goudie's estimates, obtained from values in the literature, may be biased towards the calcrete types with higher $CaCO_3$ contents, i.e. hardpan and powder calcretes. All the analyses in Table 26 compare well with Netterberg's (1969(b), p. 111) calcified sands, which he regards as fairly immature calcrete.

The purpose of the analyses in Table 29 was to determine whether rapid trace element analyses on a whole-rock basis could be applied to regional exploration in calcretes to assist in the location of potential target areas of uranium mineralization. From the elements analyzed, vanadium has the highest variability and concentrations due

to the presence of carnotite. There is no other significant element that can be used as a tracer for uranium. Many elements have concentrations below their detection limits, but data of this type are nevertheless useful because they provide an upper limit to their concentration in calcrete.

TABLE 31: WORLD AVERAGE VALUES FOR CALCRETE (Goudie, 1972, p. 450)

Element	%
CaO	42,6
SiO_2	12,3
Al_2O_3	2,1
Fe_2O_3	2,0
MgO	3,1
$CaCO_3$	79,3

14.3 Factor Analysis

Factor analysis was applied to the data in Table 30. Only chemical analyses were treated in this manner. Mineralogical proportions were ignored because the element distributions are primarily controlled by the absence or presence of minerals or discrete phases. Correct interpretation of the factors will therefore yield the precipitation history of the epigenetic minerals and the related processes.

TABLE 32: CORRELATION MATRICES OF THIRTEEN SAMPLES OF THE EPIGENETIC FRACTION OF THE CALCRETES FROM THE LANGER HEINRICH
(a) UNTRANSFORMED DATA
(b) LOG-TRANSFORMED DATA

(a) CORRELATION MATRIX OF 13 SAMPLES

NO TRANSFORMATION

	MEAN	STD DEV	SiO_2	Al	Fe	MgO	CaO	Na_2O	K_2O	Ba	Ce	Co	Dy	Eu	La	Lu	Pb	Sc	Sm	Sr	U	V	Yb
SiO_2	0.189D 01	0.107D 01	1.000	0.220	0.471	-0.071	-0.482	0.110	0.204	-0.250	0.456	0.152	0.407	0.472	0.484	0.407	-0.007	0.763	0.423	-0.190	-0.196	-0.185	0.582
Al	0.313D 01	0.151D 01	0.220	1.000	0.868	0.109	-0.796	0.368	0.935	0.582	0.880	0.697	0.436	0.877	0.812	0.653	0.520	0.582	0.908	0.286	-0.020	0.153	0.755
Fe	0.274D 01	0.152D 01	0.471	0.868	1.000	0.024	-0.716	0.211	0.687	0.384	0.915	0.709	0.448	0.776	0.866	0.620	0.153	0.592	0.875	0.445	-0.162	-0.014	0.702
MgO	0.238D 01	0.273D 01	-0.071	0.109	0.024	1.000	-0.252	0.619	0.159	0.172	0.010	0.097	-0.259	0.041	-0.004	-0.135	0.086	0.036	-0.115	-0.119	-0.272	-0.240	-0.172
CaO	0.450D 02	0.216D 01	-0.482	-0.796	-0.716	-0.252	1.000	-0.480	-0.779	-0.234	-0.685	-0.409	-0.459	-0.782	-0.629	-0.524	-0.500	-0.754	-0.696	-0.085	-0.052	-0.161	-0.728
Na_2O	0.677D 00	0.332D 00	0.110	0.368	0.211	0.619	-0.480	1.000	0.451	0.445	0.316	0.486	0.391	0.494	0.213	0.226	0.677	0.411	0.239	0.132	0.136	0.258	0.415
K_2O	0.135D 01	0.592D 00	0.204	0.935	0.687	0.159	-0.779	0.451	1.000	0.573	0.785	0.592	0.489	0.895	0.715	0.712	0.700	0.628	0.863	0.024	0.123	0.278	0.761
Ba	0.216D 03	0.246D 03	-0.250	0.582	0.384	0.172	-0.234	0.445	0.573	1.000	0.574	0.858	0.148	0.491	0.537	0.397	0.606	0.218	0.515	0.235	-0.122	0.058	0.311
Ce	0.288D 02	0.173D 02	0.456	0.880	0.915	0.010	-0.685	0.316	0.785	0.574	1.000	0.808	0.577	0.911	0.970	0.754	0.386	0.724	0.956	0.299	-0.113	0.071	0.811
Co	0.116D 02	0.779D 01	0.152	0.697	0.709	0.097	-0.409	0.486	0.592	0.858	0.808	1.000	0.399	0.671	0.755	0.525	0.462	0.469	0.721	0.401	-0.135	0.059	0.548
Dy	0.169D 01	0.103D 01	0.407	0.436	0.448	-0.259	-0.459	0.391	0.489	0.148	0.577	0.399	1.000	0.719	0.501	0.657	0.481	0.601	0.639	0.219	0.628	0.724	0.783
Eu	0.585D 00	0.308D 00	0.472	0.877	0.776	0.041	-0.782	0.494	0.895	0.491	0.911	0.671	0.719	1.000	0.848	0.817	0.642	0.803	0.935	0.144	0.122	0.295	0.932
La	0.195D 02	0.119D 02	0.484	0.812	0.866	-0.004	-0.629	0.213	0.715	0.537	0.970	0.755	0.501	0.848	1.000	0.684	0.286	0.701	0.917	00.210	-0.188	-0.017	0.770
Lu	0.152D 00	0.774D-01	0.407	0.658	0.620	-0.135	-0.524	0.226	0.712	0.397	0.754	0.525	0.657	0.817	0.684	1.000	0.481	0.561	0.798	0.169	0.150	0.262	0.758
Pb	0.977D 01	0.606D 01	-0.007	0.520	0.153	0.086	-0.500	0.677	0.700	0.606	0.386	0.462	0.481	0.642	0.286	0.481	1.000	0.501	0.449	-0.075	0.308	0.438	0.593
Sc	0.249D 01	0.149D 01	0.763	0.582	0.592	0.036	-0.754	0.411	0.628	0.218	0.724	0.469	0.601	0.803	0.701	0.561	0.501	1.000	0.704	-0.207	-0.025	0.088	0.777
Sm	0.492D 01	0.312D 01	0.423	0.908	0.875	-0.115	-0.696	0.239	0.863	0.515	0.956	0.721	0.639	0.935	0.917	0.798	0.449	0.704	1.000	0.196	0.079	0.244	0.856
Sr	0.168D 03	0.104D 03	-0.190	0.288	0.445	-0.119	-0.085	0.132	0.024	0.235	0.299	0.401	0.219	0.144	0.210	0.169	-0.075	-0.207	0.196	1.000	0.006	0.097	0.187
U	0.123D 04	0.127D 04	-0.196	-0.020	-0.162	-0.272	-0.052	0.136	0.123	-0.122	-0.113	-0.135	0.628	0.122	-0.188	0.150	0.308	-0.025	0.079	00.006	1.000	0.975	0.187
V	0.316D 03	0.250D 03	-0.185	0.153	-0.014	-0.240	-0.161	0.258	0.278	0.058	0.071	0.059	0.724	0.295	-0.017	0.262	0.438	0.088	0.244	0.097	0.975	1.000	0.330
Yb	0.110D 01	0.599D 00	0.582	0.755	0.702	-0.172	-0.728	0.415	0.761	0.311	0.811	0.548	0.783	0.932	0.770	0.758	0.593	0.777	0.856	0.187	0.187	0.330	1.000

(b) CORRELATION MATRIX OF 13 SAMPLES

LOG TRANSFORMATION

	MEAN	STD DEV	SiO_2	Al	Fe	MgO	CaO	Na_2O	K_2O	Ba	Ce	Co	Cy	Eu	La	Lu	Pb	Sc	Sm	Sr	U	V	Yb
SiO_2	0.157D 00	0.258D 00	1.000	0.030	0.234	-0.085	-0.897	0.235	0.067	-0.176	0.216	0.183	0.448	0.317	0.262	0.167	0.020	0.625	0.204	-0.251	-0.139	-0.228	0.437
Al	0.447D 00	0.217D 00	0.030	1.000	0.915	0.325	-0.775	0.497	0.936	0.724	0.839	0.714	0.483	0.823	0.738	0.596	0.582	0.472	0.864	0.510	-0.138	0.270	0.704
Fe	0.382D 00	0.225D 00	0.234	0.915	1.000	0.263	-0.700	0.459	0.791	0.696	0.874	0.814	0.501	0.782	0.763	0.580	0.382	0.478	0.863	0.457	-0.257	0.105	0.679
MgO	0.203D 00	0.377D 00	-0.086	0.325	0.263	1.000	-0.444	0.571	0.365	0.351	0.149	0.292	-0.148	0.195	0.168	-0.001	0.212	0.202	0.033	0.028	-0.279	-0.063	-0.062
CaO	0.165D 01	0.211D-01	-0.397	-0.775	-0.700	-0.444	1.000	-0.517	-0.780	-0.426	-0.608	-0.491	-0.457	-0.694	-0.577	-0.407	-0.510	-0.711	-0.629	-0.219	0.172	-0.144	-0.594
Na_2O	-0.219D 00	0.220D 00	0.235	0.497	0.459	0.571	-0.517	1.000	0.555	0.645	0.506	0.715	0.409	0.627	0.451	0.328	0.728	0.601	0.410	0.141	-0.156	0.128	0.531
K_2O	0.900D-01	0.193D 00	0.067	0.936	0.791	0.365	-0.780	0.555	1.000	0.653	0.754	0.648	0.544	0.844	0.645	0.666	0.749	0.575	0.836	0.323	-0.030	0.358	0.689
Ba	0.213D 01	0.418D 00	-0.176	0.724	0.696	0.351	-0.426	0.645	0.653	1.000	0.804	0.867	0.410	0.727	0.731	0.605	0.639	0.338	0.726	0.499	-0.234	0.207	0.605
Ce	0.139D 01	0.251D 00	0.216	0.839	0.874	0.149	-0.608	0.506	0.754	0.804	1.000	0.840	0.609	0.932	0.927	0.722	0.543	0.584	0.921	0.447	-0.321	0.067	0.870
Co	0.965D 00	0.319D 00	0.183	0.714	0.814	0.292	-0.491	0.715	0.648	0.867	0.840	1.000	0.467	0.762	0.772	0.521	0.580	0.598	0.793	0.219	-0.372	0.031	0.673
Dy	0.166D 00	0.231D 00	0.448	0.483	0.501	-0.148	-0.457	0.409	0.544	0.410	0.609	0.467	1.000	0.707	0.562	0.623	0.521	0.523	0.691	0.315	0.431	0.609	0.727
Eu	-0.290D 00	0.236D 00	0.317	0.823	0.782	0.195	-0.694	0.627	0.844	0.727	0.932	0.762	0.707	1.000	0.838	0.807	0.743	0.692	0.900	0.347	-0.181	0.179	0.931
La	0.122D 01	0.247D 00	0.262	0.738	0.763	0.163	-0.577	0.451	0.645	0.731	0.927	0.772	0.562	0.838	1.000	0.515	0.422	0.623	0.852	0.324	-0.334	0.040	0.839
Lu	-0.888D 00	0.285D 00	0.167	0.596	0.580	-0.001	-0.407	0.328	0.666	0.605	0.722	0.521	0.623	0.807	0.515	1.000	0.636	0.331	0.723	0.414	-0.015	0.215	0.700
Pb	0.927D 00	0.231D 00	0.020	0.582	0.382	0.212	-0.510	0.728	0.749	0.639	0.543	0.580	0.521	0.743	0.422	0.636	1.000	0.591	0.606	0.116	0.041	0.364	0.651
Sc	0.331D 00	0.246D 00	0.625	0.472	0.478	0.202	-0.711	0.601	0.575	0.338	0.584	0.598	0.523	0.692	0.623	0.331	0.591	1.000	0.595	-0.261	-0.321	-0.070	0.672
Sm	0.613D 00	0.274D 00	0.204	0.864	0.863	0.033	-0.629	0.410	0.836	0.726	0.921	0.793	0.691	0.900	0.852	0.723	0.606	0.595	1.000	0.309	-0.100	0.295	0.846
Sr	0.209D 01	0.444D 00	-0.251	0.510	0.457	0.028	-0.219	0.141	0.323	0.499	0.447	0.219	0.315	0.347	0.324	0.414	0.116	-0.261	0.309	1.000	0.176	0.315	0.335
U	0.269D 01	0.730D 00	-0.139	-0.138	-0.257	-0.279	0.172	-0.156	-0.030	-0.234	-0.321	-0.372	0.431	-0.181	-0.334	-0.015	0.041	-0.321	-0.100	0.176	1.000	0.875	-0.140
V	0.237D 01	0.351D 00	-0.228	0.270	0.105	-0.063	-0.144	0.128	0.358	0.207	0.067	0.031	0.609	0.179	0.040	0.215	0.364	-0.070	0.295	0.315	0.875	1.000	0.142
Yb	-0.269D-01	0.267D 00	0.437	0.704	0.679	-0.062	-0.594	0.531	0.689	0.605	0.870	0.673	0.727	0.931	0.839	0.700	0.651	0.672	0.845	0.335	-0.140	0.142	1.000

CONFIDENTIAL

Table 32 gives the correlation matrices for both normal and log-transformed data. Summaries of the two correlation matrices for the data below the diagonal are given in Table 33. For thirteen samples the 99 per cent and 95 per cent confidence limits are ± 0,7 and ± 0,56 respectively. Those elements with an asterisk denote the ones which are not correspondingly represented in either Table 32(a) or 32(b). For example, sodium in the normal untransformed data shows no significant correlation with the elements barium, europium, lanthanum and scandium as is found for the log-transformed data. In general though, most elements are correspondingly represented, but for those that are not, others act as synonyms, e.g. the rare-earth elements behave as a coherent group and therefore the correlation of one of the elements infers the presence of the others. As there is no significant deviation from normality the normal untransformed data were used in the factor analysis.

In the varimax factor matrix (Table 34) six coherent factors account for 94,1 per cent of the total variance of all the major and trace elements. The percentage contribution of each factor is calculated by dividing the sum of squares within each factor by the total sum of squares multiplied by the percentage variance, e.g. variance for factor 1 = (8,6/19,8) x 94,1 = 40,9 % (See Table 34 for the values above).

The loading of each element in all the factors gives the fraction of variance of every element that is explained by the factors. High loadings of a group of elements within a factor specify a covariant behaviour of those elements, e.g. alumina, iron oxide, potassium oxide, cerium, etc. in factor 1.

TABLE 33: SUMMARIES OF CORRELATION MATRICES IN TABLE 32
(a) UNTRANSFORMED DATA
(b) LOG-TRANSFORMED DATA

(a)

	99 %	95 %	99 %	95 %
	+	+	-	-
SiO_2	Sc	Yb*		
Al_2O_3	Fe_2O_3, K_2O, Ce, Eu, La, Sm, Yb		CaO	
Fe_2O_3	Ce, Co, Eu, La, Sm, Yb	K_2O, Lu, Sc*	CaO	
MgO		Na_2O		
CaO			K_2O, Eu, Sc, Yb*	Ce, La, Sm
Na_2O		Pb		
K_2O	Ce, Eu, La, Sm, Yb	Lu, Pb		
Ba	Co	Ce, La, Pb		
Ce	Co, Eu, La, Lu, Sc, Sm, Yb	Dy		
Co	La, Sm	Eu		
Dy	Eu, Lu, Sc*, Sm, V, Yb	U*		
Eu	La, Lu, Sc, Sm, Yb	Pb		
La	Lu, Sc, Sm, Yb			
Lu	Sm, Yb	Sc*		
Pb		Yb		
Sc	Sm, Yb			
Sm	Yb			
Sr				
U	V			

* Elements NOT correlated with the element in question for the log-transformed data

Confidence limits at n = 13

99 % = ± 0,7
95 % = ± 0,56

(b)

	99 %	95 %	99 %	95 %
	+	+	-	-
SiO_2		Sc		
Al_2O_3	Fe_2O_3, K_2O, Ba, Ce, Co, Eu, La, Sm, Yb	Lu, Pb*	CaO	
Fe_2O_3	K_2O, Ce, Co, Eu, La, Lu, Sm, Yb		CaO	
MgO		Na_2O		
CaO			K_2O, Sc	Ce, Eu, La, Sm
Na_2O	Co*, Pb	Ba*, Eu*, La*, Sc*		
K_2O	Ce, Eu, La, Pb, Sm	Ba*, Co*, Lu, Yb		
Ba	Ce, Co, Eu*, La, Sm*	Lu, Pb, Yb*		
Ce	Co, Eu, La, Lu, Sm, Yb	Dy, Sc		
Co	Eu, La, Sm	Pb*, Sc*, Yb*		
Dy	Eu, Yb	La*, Lu, Sm, V		
Eu	La, Lu, Pb, Sm, Yb	Sc		
La	Sm, Yb	Lu, Sc		
Lu	Sm, Yb	Pb*		
Pb		Sc*, Sm*, Yb		
Sc		Sm, Yb		
Sm	Yb			
Sr				
U	V			

* Elements NOT correlated with the element in question for the untransformed data.

Confidence limits at n = 13

99 % = ± 0,7
95 % = ± 0,56

CONFIDENTIAL

TABLE 34: VARIMAX MATRIX OF THIRTEEN SAMPLES OF THE EPIGENETIC FRACTION OF THE CALCRETES FROM THE LANGER HEINRICH

VARIMAX MATRIX ACCOUNTING FOR 94,1 PER CENT OF TOTAL PROBLEM VARIANCE

NO TRANSFORMATION

	FACTOR	1	2	3	4	5	6
SUM OF SQUARES		8.606	3.116	1.928	2.368	1.472	2.268
0.975	SiO_2	0.359	0.151	0.014	0.226	-0.099	-0.873
0.983	Al	0.951	-0.053	-0.160	-0.197	0.088	0.071
0.973	Fe	0.881	0.122	-0.031	-0.030	0.380	-0.191
0.892	MgO	0.009	0.271	-0.895	-0.003	-0.049	0.120
0.895	CaO	-0.801	0.127	0.418	-0.113	0.068	0.212
0.989	Na_2O	0.151	-0.265	-0.816	-0.412	0.077	-0.232
0.982	K_2O	0.888	-0.203	-0.216	-0.253	-0.195	0.058
0.982	Ba	0.400	0.061	-0.129	-0.861	0.083	0.231
0.978	Ce	0.878	0.039	0.001	-0.302	0.201	-0.271
0.939	Co	0.553	0.071	-0.104	-0.697	0.336	-0.132
0.973	Dy	0.428	-0.710	0.048	-0.141	0.172	-0.483
0.978	Eu	0.855	-0.236	-0.137	-0.271	-0.014	-0.313
0.920	La	0.846	0.137	0.068	-0.274	0.147	-0.291
0.714	Lu	0.707	-0.241	0.139	-0.259	0.012	-0.264
0.899	Pb	0.356	-0.457	-0.317	-0.593	-0.330	-0.051
0.936	Sc	0.623	-0.062	-0.156	-0.133	-0.260	-0.659
0.982	Sm	0.927	-0.133	0.100	-0.233	0.068	-0.189
0.925	Sr	0.168	-0.081	0.006	-0.098	0.929	0.132
0.963	U	-0.040	-0.971	0.060	0.089	-0.021	0.079
0.965	V	0.099	-0.973	0.016	-0.051	0.036	0.068
0.916	Yb	0.750	-0.320	-0.013	-0.181	0.034	-0.466

Opposite signs indicate opposing covariances between the variables, e.g. alumina and calcium oxide.

Factor 1: Lithification

Factor 1 has the highest variability explained and therefore is statistically the most significant. Positive loadings are given for alumina, iron oxide, potassium oxide, cerium, europium, lanthanum, lutetium, samarium, ytterbium and scandium. On the negative side calcium oxide is found. Essentially this factor is one where the rare earths, alumina and iron oxide are leached and then co-precipitated, for they occur as a coherent group. Opposing this process was the epigenetic introduction of calcium which precipitated as calcite, thereby cementing the breccia. The overall abundance of calcite is so great that it acts as a diluting medium for the first-mentioned groups.

Owing to the limited solubility of the rare earths, scandium, aluminium and iron in weekly alkaline environments (Table 19), they are precipitated as hydroxides and are adsorbed onto clays (Roaldset, 1967). This last point is particularly important and will be dealt with further when the geochemistry of the individual and groups of elements is discussed.

Factor 2: Carnotite Precipitation

Both uranium and vanadium are rated with the highest negative loadings, followed by a slightly lower loading on dysprosium. Uranium and vanadium behave coherently with the

precipitation of carnotite from solution. Interpretation of the relation with dysprosium is more subtle. Factor loadings on dysprosium are distributed between factors 1, 2 and 6. Although in the first and last cases the loadings are fairly low, attention must nevertheless be focused on them. The effect produced is referred to here as the dysprosium anomaly.

Dysprosium would be expected to behave in a coherent manner with the other rare earths and be associated with factor 1. However, as it forms a coherent variable with uranium and vanadium, this implies that the precipitation of carnotite may be related to the presence of clays or hydrated oxides of iron or aluminium which formed the nucleating seed upon which the uranyl ion became attached.

Factor 3: Ion Exchange Properities and Formation of Clays

Clays associated with the calcrete are of the montmorillonite-smectite varieties. High factor loadings on both sodium and magnesium suggest an ion exchange mechanism: possibly two Na^{+} ions are exchanged for each Mg^{2+} ion within the structural lattice of the authigenic clays.

Another important mechanism that can also account for this relationship is the formation of montmorillonite *in situ* by the reaction of magnesium ions on plagioclase feldspars.

Factor 4: Substitution in Calcite Lattice

Barium, cobalt and lead are capable of substituting in the calcite lattice. High factor loadings on these elements suggest that this has happened in this case.

↑ see heading 220

Factor 5: Substitution in Calcite Lattice

This factor has the lowest variance, signifying its lack of importance. Strontium substitutes for calcium in the calcite lattice. It seems likely that strontium behaves differently from barium, cobalt and lead during substitution, and therefore has its own factor.

Factor 6: Silica

Silica and scandium have high factor loadings. Scandium also occurs in factor 1 and therefore factor 6 suggests that a certain amount of silica was released from biotite in the detrital material or from the clays during postdiagenetic leaching.

Factor analysis of the raw data provided pointers concerning the nature and mechanisms which were involved during the formation of the calcrete. The calcite and carnotite were precipitated as independent phases within the pore spaces of the detrital material from mineralized sub= surface waters. Simultaneously iron, aluminium and the rare earths were leached from the detrital material and co-precipi= tated as hydroxides on montmorillonite. The influence of clay on the precipitation of carnotite was noted.

Following the orthogonal varimax matrix, the vectors were rotated, from which the promax matrix was computed for up to five degrees of obliquity (KMIN = 5). This process simplifies the interpretation of the problem and allows correlations between the factors to be obtained, which was not possible from the varimax method.

TABLE 35: PROMAX MATRIX OF THIRTEEN SAMPLES OF THE EPIGENETIC FRACTION OF THE CALCRETES FROM THE LANGER HEINRICH

PROMAX OBLIQUE REFERENCE STRUCTURE MATRIX KMIN = 5

NO TRANSFORMATION

FACTOR	1	2	3	4	5	6
SiO_2	0.032	0.261	-0.008	0.300	0.113	-0.837
Al	0.728	-0.023	-0.064	-0.034	0.046	0.227
Fe	0.612	0.122	-0.029	0.112	0.319	-0.059
MgO	0.028	0.235	-0.870	0.055	0.047	0.061
CaO	-0.590	0.100	0.348	-0.293	0.033	0.098
Na_2O	-0.185	-0.136	-0.747	-0.246	0.153	-0.167
K_2O	0.663	-0.122	-0.067	-0.085	-0.215	0.217
Ba	0.113	0.200	0.001	-0.785	-0.003	0.339
Ce	0.492	0.137	0.064	-0.151	0.121	-0.113
Co	0.126	0.212	-0.037	-0.577	0.246	0.001
Dy	0.048	-0.575	0.078	0.033	0.184	-0.313
Eu	00.461	-0.103	-0.033	-0.084	-0.047	-0.139
La	0.482	0.233	0.128	-0.147	0.055	-0.149
Lu	0.375	-0.120	0.221	-0.124	-0.048	-0.104
Pb	0.047	-0.261	-0.142	-0.453	-0.318	0.079
Sc	0.204	0.117	-0.068	0.010	-0.276	-0.548
Sm	0.598	-0.042	0.187	-0.078	-0.005	-0.012
Sr	0.075	-0.177	-0.110	-0.034	0.901	0.196
U	-0.023	-0.957	0.088	0.179	0.060	0.176
V	0.031	-0.931	0.063	0.070	0.103	0.197
Yb	0.340	-0.181	0.058	-0.004	0.005	-0.296

TABLE 36: CORRELATION MATRIX OF FACTORS IN THE PROMAX MATRIX OF TABLE 35

CORRELATIONS BETWEEN PROMAX PRIMARY FACTORS KMIN = 5

NO TRANSFORMATION

FACTOR	1	2	3	4	5	6
1	1.000	-0.324	-0.205	-0.645	0.155	-0.661
2	-0.324	1.000	0.153	0.450	0.124	0.431
3	-0.205	0.153	1.000	0.276	0.250	0.099
4	-0.645	0.460	0.276	1.000	-0.114	0.530
5	0.155	0.124	0.250	-0.114	1.000	-0.101
6	-0.661	0.431	0.099	0.530	-0.101	1.000

Table 35 gives the promax matrix and Table 36 the correlation matrix between the promax factors. Essentially, the six factors remain as they were for the varimax but with successive rotations some of the weaker factor loadings are eliminated, thereby accentuating the stronger ones. However, with too many rotations the loadings on the variables become insignificant which results in much stronger correlations between the factors. This situation then becomes meaningless. An optimum number of rotations must be selected so that the interpretation remains relevant. At KMIN 5, loadings on all the rare earths with the exception of samarium are low. Here again is a case where interpretation must allow for synonyms, and samarium is regarded as being representative of the other rare earths.

Factors 1 and 4 are negatively correlated (Table 36) which suggests barium, cobalt and lead substitute in the calcite lattice. Factors 1 and 6 are positively correlated which indicates that silica, alumina, iron oxide, etc. have a common source.

14.4 Geochemistry of Individual Elements or Groups of Elements

Factor analysis has broadly established the nature of the mechanisms involved during the lithification of the breccia-conglomerate to produce a hard, indurated calcrete. Limited detail was provided concerning the actual mechanisms involved in the six factors and the geochemical parameters controlling the distribution of the elements. The geochemistry of individual and groups of elements is discussed with the

possible implications for the development of calcrete duricrust deposits.

14.4.1 Iron

Iron is distributed throughout the Gemsbok and Langer Heinrich calcrete formations. The colour of the pigmentation varies from yellowish-brown to red, implying that there are different degrees of oxidation of the iron.

The source of the iron lies in the alteration and decomposition of iron-bearing minerals such as biotite and hornblende from the Tinkas Formation and Bloedkoppie Granite. Haloes of red staining surrounding biotite crystals have been clearly observed in the Bloedkoppie Granite. Similar phenomena have been reported by Walker (1967) from the deserts of Colorado, where the halo is composed of minute euhedral grains of hematite. Complete alteration of these femic minerals results in the formation of authigenic montmorillonite, iron oxides and calcite. The release of iron is controlled by the Eh and pH of the water acting upon the mineral.

Depending on the oxidation potential, either soluble iron (II) is released to solution or *in situ* precipitation of iron (III) in the hydroxide form takes place. Those sediments with a greater proportion of iron (II) will be drab as opposed to the red colouration of the oxidized iron (III). There are three main forms of iron oxide pigment present in red beds (*ibid.*, p. 360):

(a) yellowish to reddish-yellow, amorphous ferric hydrate,

(b) amorphous red ferric hydrate,

(c) crystallized red hematite.

The conversion from the amorphous to the crystalline states is a time-dependent factor.

Iron is closely associated with the interstitial clays. Walker (ibid.) notes the existence of an iron-rich montmorillonite in red beds. Similarly Spencer et al (1969, p. 991) concluded that the ferric hydroxides occur in the finer fraction of some marine sediments.

Ferric hydroxide precipitates at a pH above 3,0 and acts as a good scavenger for the transition metals and the rare earths.

The iron contents of the acid-soluble fraction of the samples have a maximum value of 6,6 per cent and a low value of 1,1 per cent (Table 30). Sample HJ2-3 was taken at a depth of 1,5 m which indicates that very strong oxidizing conditions occur near the surface, thereby precipitating the iron in the red hydroxide form.

14.4.2 Alumina and silica

The main source of these species in the calcrete is the decomposition of hydrolysis of the feldspars, chiefly microcline and albite. Thermodynamics predicts (Helgeson et al, 1969, p. 463) that the following reaction will take place during the hydrolysis of coexisting albite and microcline.

$$KAlSi_3O_8 + NaAlSi_3O_8 + 16H_2O \rightarrow 2Al(OH)_4^- + K^+ + Na^+ + 6H_4SiO_4 \quad (14.1)$$

This equation therefore accounts for tetrahydroxo-aluminate (III) and silicic acid which can be precipitated from subsurface waters in moderately alkaline conditions. Sodium and potassium ions are likewise liberated in this reaction.

Amorphous silica in the form of silicic acid, formed in equation (14.1), has a solubility of 100 to 140 ppm at 25 °C in water (Morey et al, 1964, p. 1995). Due to this low solubility, the silica released is quickly precipitated and will establish the following equilibrium conditions, (ibid., p. 2001):

$$SiO_{2\,(\text{amorphous solid})} + nH_2O \rightleftarrows SiO_{2\,(aq)} \qquad (14.2)$$

Mackenzie and Garrels (1965, p. 57) reported that some montmorillonites can release up to 21 ppm silica to seawater after six months, with the residue consisting of hydrated alumina. This indicates a preferential removal of silica with respect to alumina. Although the subsurface water at the Langer Heinrich is not as saline as seawater, a reaction would nevertheless occur at possibly a reduced rate. Fig. 57 is a plot of Al_2O_3 versus Fe_2O_3 and shows a good correlation (correlation coefficient = 0,87) between both oxides. It is suggested therefore that through the decomposition of minerals such as the feldspars and the iron-rich montmorillonite as described by Walker (1967), silicic acid is dissolved, leaving a residue of hydrated iron (III) ions and tetrahydroxo-aluminate (III). Ions of this type are capable of co-precipitating metals, viz. the rare earths in alkaline solutions.

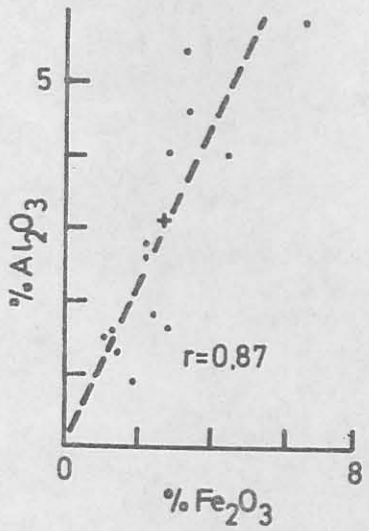

Fig. 57: Variation diagram of Al_2O_3 plotted against Fe_2O_3 (correlation coefficient r = 0,87) for the epigenetic fraction of the calcretes. (+ = mean).

14.4.3 Potassium, sodium and magnesium

These elements are generally involved in reactions and ion exchange processes in the clays of the calcrete. Factor analysis demonstrated this clearly and is corroborated by Graf (1960).

High correlation coefficients of potassium with the alumina, iron (III) oxide and rare earths are observed in Table 32(a). Potassium is probably involved largely with the ion exchange properties of the montmorillonite.

Consideration must now be given to the origin of montmorillonite clay. Montmorillonite is an authigenic mineral, having largely been formed in situ by the reaction of magnesium with albitic feldspar. The flow-rate of sub= surface water is an important factor (Berner, 1971, p. 173). Under almost stagnant conditions, which would be expected

in the subsurface water at the Langer Heinrich, a slow reaction between hydrated alumina, silica and certain cations takes place. The reaction can be considered in the following manner:

$$Mg^{2+} + 3NaAlSi_3O_8 + 4H_2O \rightarrow 2Na_{0,5}\,Al_{1,5}\,Mg_{0,5}\,Si_4O_{10}(OH)_2 + 2Na^+ + H_4SiO_4 \qquad (14.3)$$

The reactants, magnesium ions, albite and water combine to form the montmorillonite, releasing sodium ions and silicic acid to the aqueous phases.

The question why there is no kaolinite present at the Langer Heinrich may arise. According to Berner (ibid.) the formation of kaolinite is related to high flow-rates of sub= surface water in regions of greater rainfall. In humid, tropical climates the slow reaction given above cannot take place due to the removal of all reaction cations in solution, leaving a residue of hydrated alumina, eventually forming bauxites. Bicarbonate ions in solution are one of the chief agents in weathering and Garrels (in Berner, 1971, p. 175) has shown that montmorillonite can only form where the HCO_3^- content approaches 100 ppm.

Magnesium is freely interchangeable with calcium in calcite, and should the substitution proceed, the mineral dolomite will form. Table 30 shows that the magnesium oxide content is generally low, but one sample (AD1-8) has 10,8 per cent. Dolomite obviously has not formed, but in the latter case it might be referred to as a magnesian calcite. In

Table 32(a) MgO has an insignificant correlation coefficient with CaO. The ratio MgO/CaO versus percentage MgO gives a parabolic curve (Fig. 58).

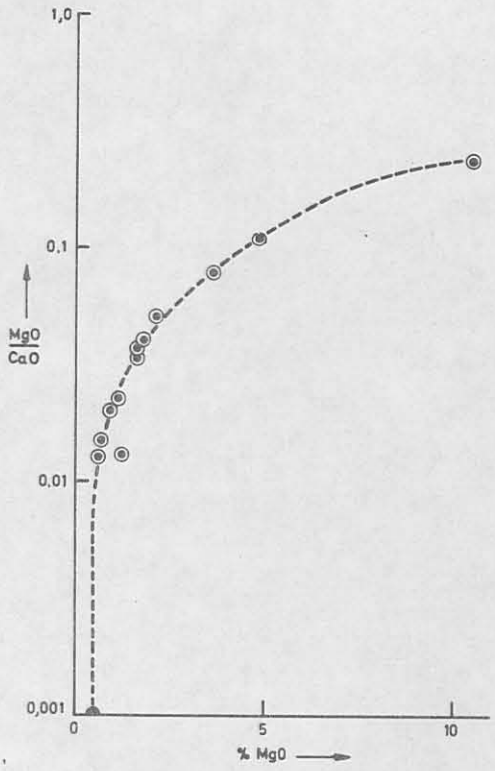

Fig. 58: The relationship between magnesium and calcium in epigenetic calcite as demonstrated by plotting the ratio MgO/CaO against MgO.

This indicates that there is a relationship of some sort between magnesium and calcium, but there has not been a systematic linear substitution of these elements with respect to each other. In other words magnesium in calcite also occurs in another form, e.g. clay. Wieder and Yaalon (1974, p. 118) found that an increase in calcium (i.e. calcite) was accompanied by a decrease in aluminium, magnesium and iron (i.e. clay). Electron probe studies by them revealed that these three elements were displaced to the fringes of crystallizing calcite. This situation would alter the

distribution of magnesium in the calcite, creating the relationship illustrated in Fig. 58.

14.4.4 The rare-earth elements

The distribution of the rare earths in the epigenetic calcite is governed by the scavenging of aluminium and iron (III) hydroxides which were adsorbed on montmorillonite, as demonstrated by the relationships in factor 1. Similar conclusions were reached by Roaldset (1973) who found that the rare earths were adsorbed under neutral and moderately alkaline conditions onto clay minerals, but at a lower pH desorption took place.

The relative abundances of the rare earths in calcretes of the Langer Heinrich, and sediments from other parts of the world, plotted as percentages of the total rare-earth concentrations, are shown in Fig. 59. Clearly the percentage abundances in both figures are very similar. The lighter rare earths, that is, lanthanum and cerium, are by far the most abundant elements and collectively comprise between 70 to 90 per cent of the total content. Cerium is the most abundant element whereas europium and lutetium are the least abundant.

Normalizing the rare-earth abundances to a composite of twenty chondritic meteorites, the relative distribution of the elements can be studied. Fig. 60 is a plot of some of the epigenetic calcite samples and limestones from the Russian Platform. The most striking feature is the uni= formity of distribution of the rare-earth patterns.

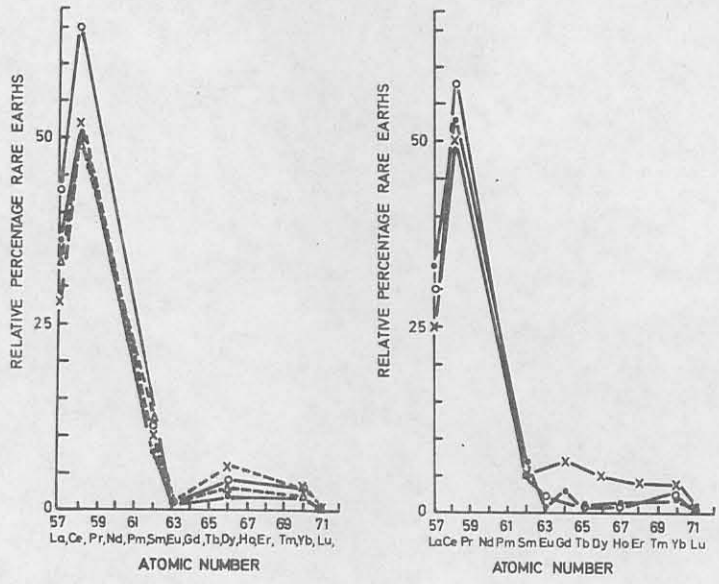

Fig. 59: Relative percentage rare-earth concentrations in
(a) Epigenetic calcite, Langer Heinrich.
(· = HJ2-3, o = HJ2-5, x = HJ2-13,
Δ = C5-15).
(b) Sediments from other parts of the world.
· = Belders Formation marble, USA;
x = average, 11 025 limestones from the Russian Platform;
o = composite 40 North American shales.
(Herrmann, 1970).

Fractionation between the lighter and heavier elements has taken place. The limestones from the Russian Platform have a rare-earth pattern very similar to those of the calcites from the Langer Heinrich. A more diagnostic approach in studying the fractionation patterns of the rare earths is to divide the concentrations of the light rare-earth by the heavy rare-earth concentrations. The function used here was (La + Ce)/(Yb + Lu) which was a modification of the function used by Balashow et al (1964, p. 951). The relationships between this ratio and total rare-earth content

and between this ratio and percentage Fe_2O_3 are shown in Fig. 61, where the overall trend appears to be positive and linear.

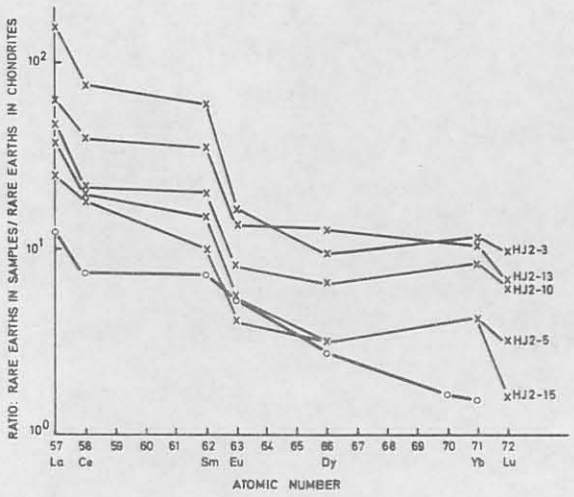

Fig. 60: Distribution patterns of rare earths, normalized to the abundances in 20 chondritic meteorites.
x = epigenetic calcite, Langer Heinrich area.
o = average, 11 025 limestones from the Russian Platform.
(Herrmann, 1970).

An increase in total rare-earth and iron contents is accompanied by an increase in the fractionation between the light and heavy rare earths. The implication was that the heavier rare earths were preferentially removed in solution to an amount of approximately 10 per cent.

Ronov et al (1967, p. 2) considered the possible mechanisms that cause the fractionation of the rare earths in nature. Basicity of the hydroxides decreases with increasing atomic number as would be expected because the ionic radii decreases due to the lanthanide contraction. This enables hydrolysis to take place at differing values of pH, thereby assisting the separation of the species.

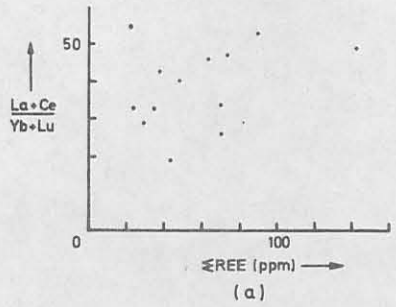

61(a)

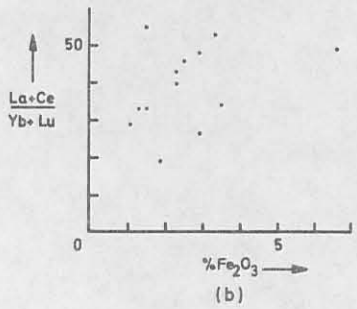

61(b)

Fig. 61: Plots of the fractionation function La + Ce/Yb + Lu against
(a) sum of the rare earths;
(b) percentage iron oxide.

A change in the oxidation state is a second causative factor. Normally rare earths are characteristically trivalent. Eu^{2+} and Ce^{4+} can occur under reducing and oxidizing conditions respectively. The desert environment of the Langer Heinrich is oxidizing, which will discount the occurrence of Eu^{2+}. Cerium (IV) behaves in a similar way to the heavier rare earths as its ionic radii decreases, thereby acquiring a stronger tendency to hydrolize and fractionate.

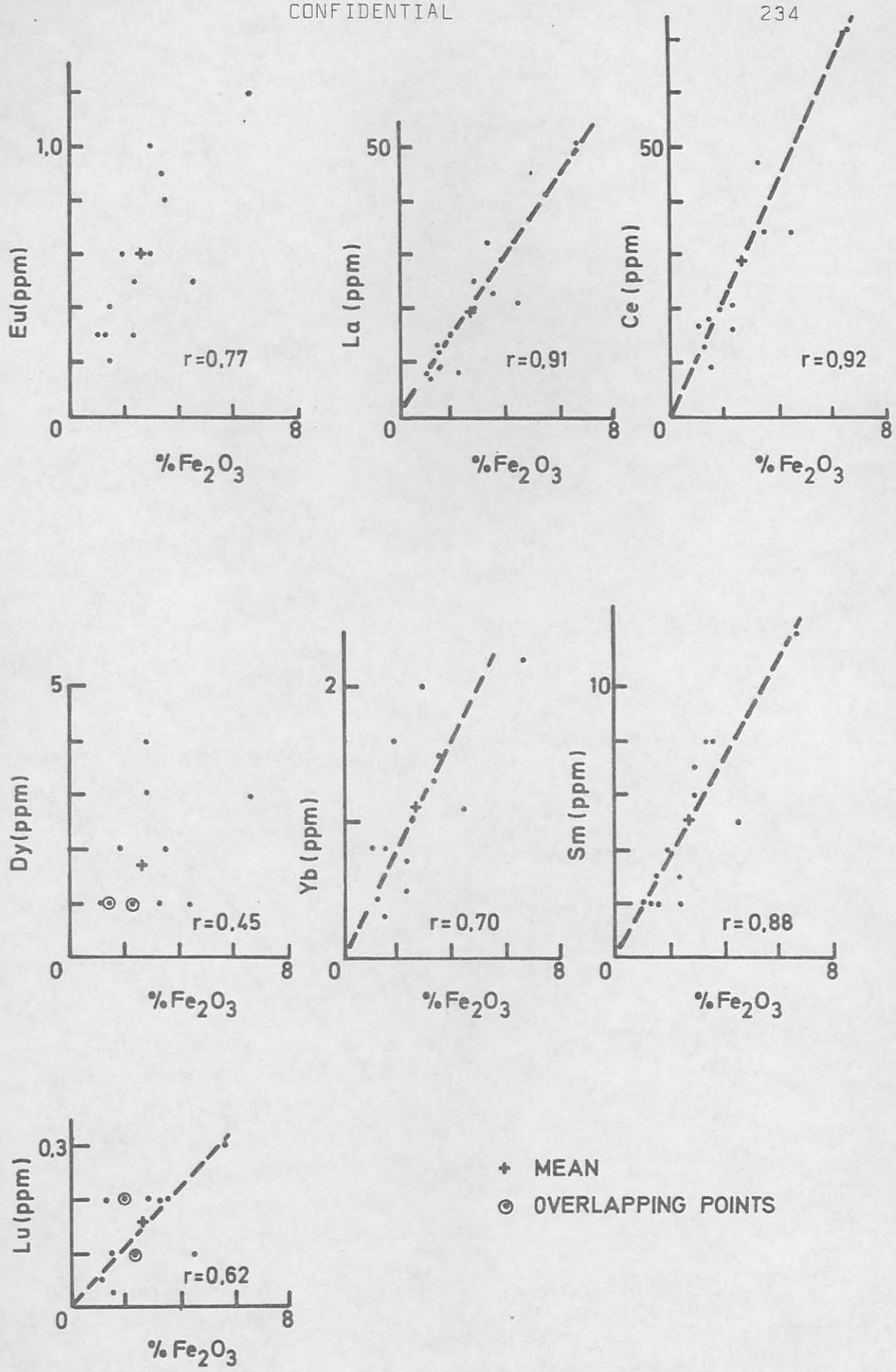

Fig. 62: Variation diagrams of rare-earth elements plotted against percentage iron oxide.

Correlation coefficients between the rare earths and Fe_2O_3 (Fig. 62) and between rare earths and Al_2O_3 (Table 32(a)) are high, except for dysprosium. It is very clear that co-precipitation with the hydrolyzate elements has taken place. The low correlation coefficient of dysprosium with respect to Fe_2O_3 and the other rare earths (Figs. 62 and 63, and Table 32(a)) and its significant loading in factor 2 (Table 34) indicates that it behaved in an anomalous manner.

A plot of the correlation coefficients (Table 32(a)) against the rare-earth atomic numbers in Fig. 63 shows a very distinct dysprosium anomaly. In all the diagrams dysprosium seems to have a closer coherence to the heavier rare earths. No explanation can be given to account for this feature and it has not been recorded in the literature. The close relationship between uranium and vanadium with dysprosium in factor 2 (Table 34) is significant, for it suggests that the uranium mineralization may be linked with the presence of montmorillonite and the precipitated hydroxides of iron and aluminium.

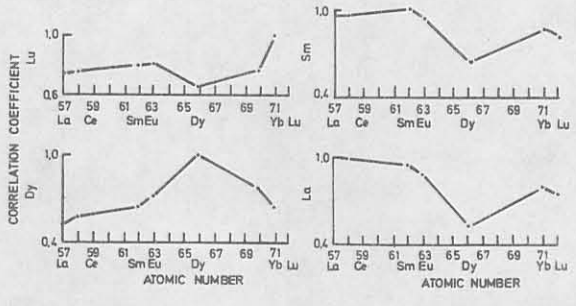

Fig. 63: Plots of the correlation coefficients of lutetium, dysprosium, samarium and lanthanum against the atomic number.

Figs. 64(a) and (b) are plots of uranium and vanadium respectively against dysprosium. Very distinct trends are observed. In both cases almost linear relationships were found in the carnotite-bearing calcretes as opposed to the unmineralized calcretes which plot much lower on the scale.

The distribution and fractionation patterns of the rare earths in the calcretes provide pointers to the chemical processes that resulted in their formation. Obviously the formation of calcrete was not purely the pre= cipitation of calcite from solution, but was accompanied by a host of syn- and post-lithification processes.

14.4.5 Vanadium and uranium

The ore deposit of the Langer Heinrich is typified by the presence of vanadium in the highest possible oxidation state, (+V). In igneous and metamorphic rocks, the latter of which includes the schists and granofelses of the Tinkas Formation, the (+III) oxidation state of vanadium is the most predominant. The source of the vandium is con= sidered to be the Tinkas Formation because it contains a high concentration of vanadium (Table 37). Vanadium concentrations in the Bloedkoppie Granite are below the 5 ppm detection limit of neutron activation analysis and therefore cannot be regarded as a significant source.

Carnotite, with the formula $K_2(UO_2)(VO_4)_2.2H_2O$, has a U/V ratio of 4,67. The U/V ratios (Table 30) have a fairly wide scatter but can be divided into two groups, the mineralized and unmineralized calcretes respectively.

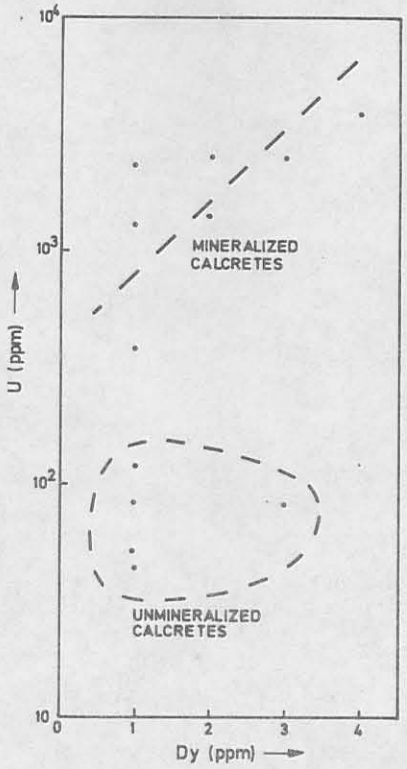

64(a)

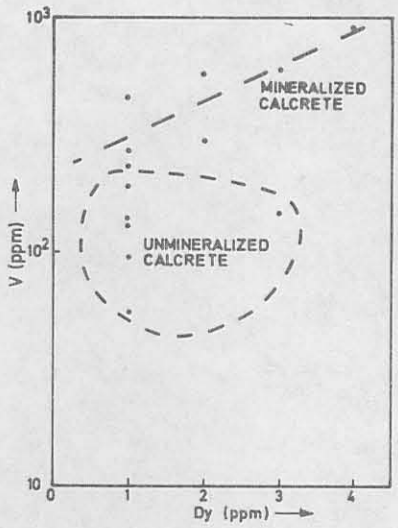

64(b)

Fig. 64: (a) Variation diagram of uranium plotted against dysprosium for both mineralized and unmineralized calcretes.
(b) Variation diagram of vanadium plotted against dysprosium for both mineralized and unmineralized calcretes.

TABLE 37: VANADIUM CONCENTRATION IN THE TINKAS FORMATION

Sample No.	V (ppm)
LH 21	128
LH 40	70
LH 41	44
LH 42	100
DJP 98	115
DJP 100	96

The former has values similar to the theoretical, whereas in the latter the ratio is much lower, indicating a relative enrichment of vanadium. A plot of uranium against vanadium is given in Fig. 65, where both groups are seen to define their own fields. The mineralized calcretes display a good correlation between uranium and vanadium, whereas unmineralized calcretes have variable ratios.

14.4.6 Geochemical mobility of the elements

Epigenetic deposits such as those found at the Langer Heinrich resulted from the supergene migration and precipitation of elements from the subsurface waters. Oxidizing conditions and a moderately alkaline environment are prerequisites which are typical of the climatic conditions in the Namib Desert. In order to gain a fuller understanding of the mechanisms involved it is necessary to devote some time to the geochemical mobility of elements during

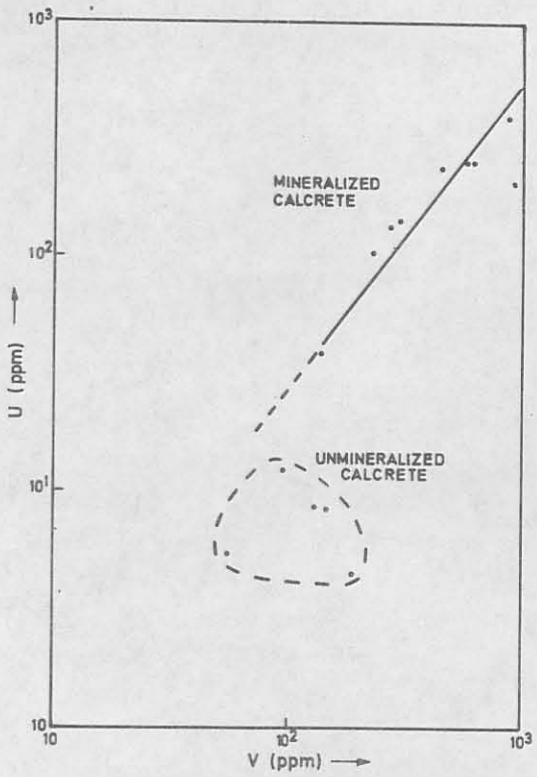

Fig. 65: Variation diagrams of uranium plotted against vanadium for both mineralized and unmineralized calcretes.

epigenetic processes in general. Dall'Aglio (1972) considered this subject in some detail and applied the fundamental concepts to studies of epigenetic uranium mineralization in Italy.

In relation to their chemical characteristics, elements will respond according to the prevailing conditions and therefore the geochemical balance in nature is governed by their geochemical behaviour. Broadly, the geochemical balance is a function of the distribution in igneous rocks, sediments and the hydrosphere. Accordingly the elements can be grouped into those which have low, medium and high

mobilities.

Fig. 66 is a measure of the geochemical mobility of the elements where the concentration within the rocks was normalized to the abundances in the hydrosphere. It was noted that when assessing the mobility of uranium and vanadium under desert conditions, they become highly mobile by oxidation and the formation of complexes, and therefore should be classed with group III. The reason for this is that the mobility of ionic complexes under supergene conditions is independent of the geochemistry of the element existing by itself.

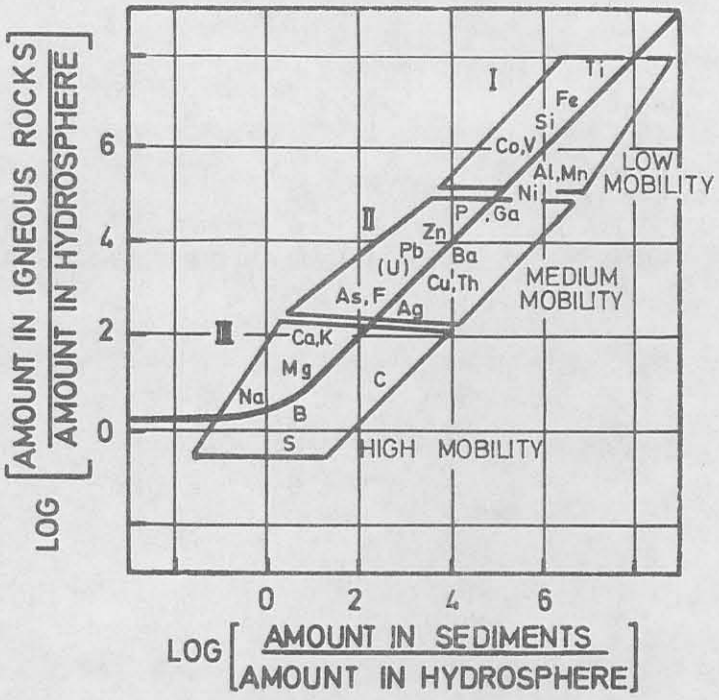

Fig. 66: Geochemical mobility of the elements in the supergene environment. (After Dall' Aglio, 1972, p. 123).

The mobility of uranium is restricted by two conditions:

(a) The manner in which it is present in the source rocks, e.g. if it is accommodated in a zircon crystal, which is resistant to weathering, there will be a minimal release of uranium. Alternatively if it is uraninite or molecules dispersed on crystal surfaces it will be more susceptible to solution.

(b) The epigenetic precipitation of insoluble minerals, in this case, carnotite.

Ronov et al (1967, p. 7) attempted to quantify these concepts in terms of the removal index, ρ.

$$\rho = \frac{Cp - Cs}{Cs}$$

Cp = concentration of an element in the parent rock, viz. Bloedkoppie Granite (Table 13). Although more than one rock type is represented at the Langer Heinrich, the Bloedkoppie Granite was selected for the parent rock because its major element composition lies between that of the rocks of the Etusis and Tinkas Formations (Table 14).

Cs = concentration of the same element in the sediment, viz. the epigenetic calcite (Table 30).

The sign of the removal index, ρ, may either be positive or negative. If it is positive the element is depleted in the calcrete, but when it is negative it is enriched in the calcrete. Graphically this is represented in Figs. 67 and 68. In both cases calcium, uranium, magnesium

and cobalt have accumulated in the calcrete and all the other elements are relatively depleted with respect to the Bloed= koppie Granite. Sample HJ2-5 (Fig. 67) has a close associa= tion between iron, scandium and the rare earths with the exception of cerium, which is depleted to a greater extent. This was not found for sample HJ2-15 (Fig. 68) as cerium occurs well within the rare-earth clustering. Similarly there is a discrepancy in the behaviour of lutetium, where the reverse is found in the respective samples.

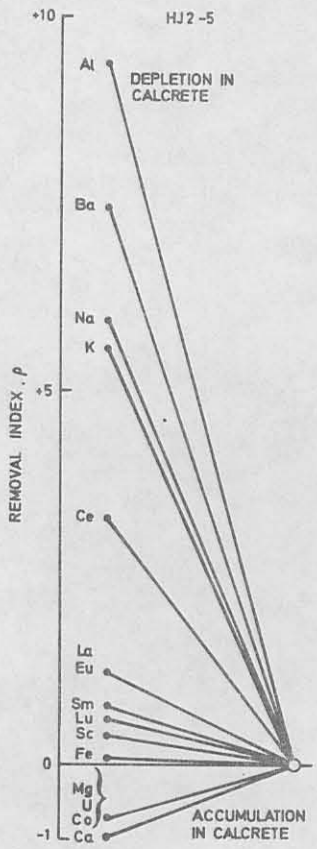

Fig. 67: The geochemical mobility of the elements in the epigenetic calcite of sample HJ2-5, with respect to the Bloedkoppie Granite. Represented in terms of the removal index.

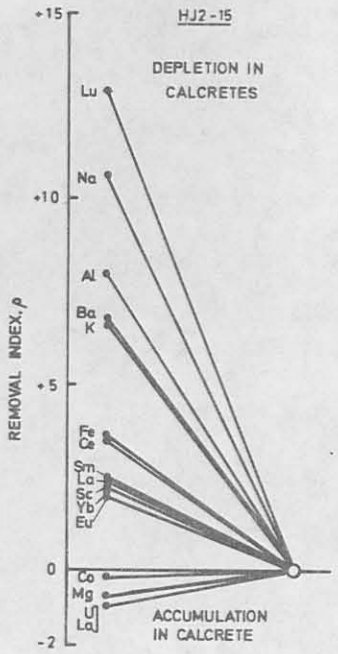

Fig. 68: The geochemical mobility of the elements in the epigenetic calcite of sample HJ2-15, with respect to the Bloedkoppie Granite. Represented in terms of the removal index.

The discrepant behaviour of cerium and lutetium in both samples can be accounted for by their depth of burial, for they were obtained from 2,5 and 7,5 m respectively (Table 27). Near the surface powerful oxidizing conditions prevailed which were sufficient to partially oxidize cerium from the (+III) to the (+IV) state. Lower down in the succession these conditions were not as severe. The stability of the lutetium inorganic complexes were greater lower down, enabling a greater fractionation to have taken place.

The elements sodium, barium and potassium were very mobile and would be expected to be relatively depleted in the calcretes.

14.5 Geochemistry and Origin of Calcrete

Uranium deposits and especially carnotite mineraliza= tion in desert, duricrust-type host rocks cannot really be re= garded as unique for it was not the calcareous cement which was the main factor in their development, but the physico-chemical relationships that were common to the precipitation of both calcite and carnotite.

An assessment of the origin of the ore-body of the Langer Heinrich requires that all the components comprising the host rock be accounted for in the model. Sediments provided the passageways through which the subsurface waters migrated and also the precipitation sites for the calcite and carnotite. The mechanism for the precipitation of the calcite is by analogy extended to the formation of the carnotite.

Netterberg (1969, p. 237, 1971, p. 9) described the origin of calcrete as being due to the process of soil suction by which calcium carbonate is precipitated in a porous sedi= ment above the water-table. Water in the pore spaces of a sediment exerts a force called the pore water pressure. Line A, Fig. 69, gives the distribution of this pressure above and below the water-table. Below the water-table the pores are saturated with water and the pore water pressure is greater than one atmosphere due to the hydrostatic head. Above the water-table the pore water pressure decreases to become less than one atmosphere and eventually zero due to capilliary action and surface tension forces, that is, the degree of pore saturation decreases upwards. The slope of line A is the suction gradient, pF, which Netterberg

defines as the negative log of the pore water pressure.

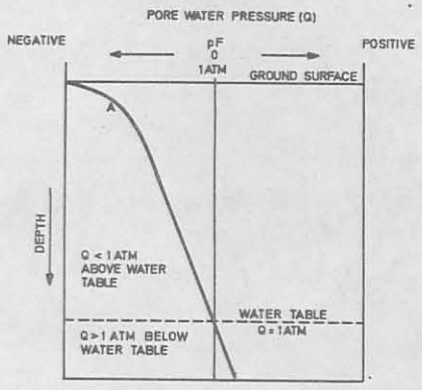

Fig. 69: Pore water pressure distribution in a sediment. (After Netterberg, 1971, p. 9).

At constant temperature, a decrease in the pore water pressure, that is, upward movement of water, will correspond to a decrease in the P_{CO_2} in equilibrium with the water, causing the precipitation of calcium carbonate. Therefore line A is a function of the solubility of calcium carbonate. Fig. 8 shows that the ore deposit has a layered structure. On a more localized scale the carnotite has precipitated in the form of concretions. Based on these facts the principles around which this discussion will centre is that the segrega= tion of carnotite resulted from a transport process, mainly upward diffusion caused by soil suction. Upward diffusion of elements in ground-water is brought about by the change in composition of the soluble components with depth. A restriction is placed on the volume of the sediment, that is, a small volume is initially required because large lateral variations in water composition are known to occur (Tables 15-18). Assume that the chemical composition of the water remains laterally constant, especially in uranium, vanadium and carbon dioxide at a specific depth. Based on this system

the vertical concentration gradients are dominant and a one-dimensional model may therefore apply. A mathematical treatment of such a system has been presented by Berner (1971, p. 25).

Vertical diffusion is a response to a chemical gradient which in this case is due to a change in the P_{CO_2}. During the formation of calcrete a decrease in P_{CO_2} will cause calcite to precipitate. When precipitation commences, concentration gradients develop and the cycle repeats itself. By analogy the precipitation of carnotite will follow the same pattern. If the detrital material is stable and upward diffusion is allowed to continue uninhibited over long periods, monomineralic layers and possibly concretions may develop. Diagramatically this process is represented in Fig. 70.

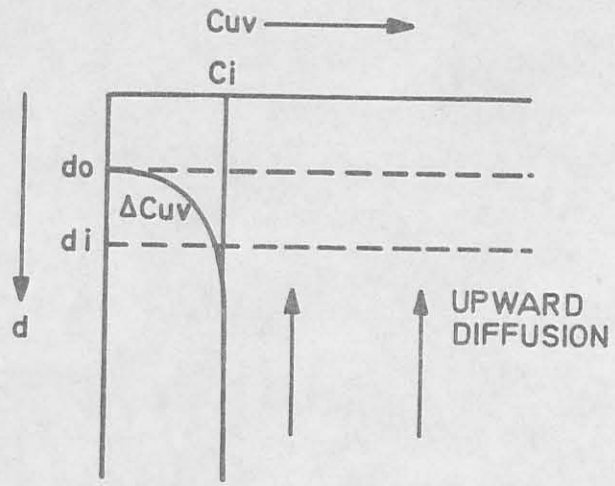

Fig. 70: Diffusion model for the formation of carnotite in layers and concretions at the Langer Heinrich. (After Berner, 1971, p. 103).

C_{uv} = concentration of UDC and vanadium in solution

d = depth of sediment

$d_1 - d_0$ = depth of sediment where the suction gradient is sufficiently high for dissociation of the UDC complex

d_1 = depth where carnotite first appears at the sediment/water interface

d_0 = depth where all uranium and vanadium have been precipitated

C_i = initial concentration of uranium and vanadium in solution

ΔC_{uv} = a generalized curve showing the change in C_{uv} with depth.

The system will operate in the following way. Below a depth of d_1 the one-dimensional system has an initial concentration of uranium, vanadium and carbon dioxide in solution, C_i. Upward diffusion of the ions continues until the depth d_1 is reached where the process of soil suction becomes operative. The uranyl dicarbonate complex will disproportionate according to equation (13.8) and carnotite will precipitate by the reaction in equation (13.10). With an increasing suction gradient and decreasing depth, the concentration of the elements in solution will follow the idealized path ΔC_{uv} until the depth d_0 is reached where all the uranium and vanadium will be consumed.

The system described is by no means so simple, as the mineralization is disjointed and occurs as possible concretionary-type accumulations (Fig. 9). Two mechanisms can be invoked to account for these phenomena.

The composition of the subsurface water is variable (Tables 15-18) over relatively short distances in which units of the one-dimensional system are closely stacked together to form a multidimensional model. Soil suction applied to such systems will lead to variations in the amount of carnotite precipitated because the composition of the water varies indiscriminately in a lateral direction. If the activities of the potassium, uranyl and vanadate ions do not reach that required for carnotite to precipitate, the ions will remain in solution. In adjacent portions of the host rocks the conditions could be favourable and carnotite will be precipitated, resulting in disjointing.

The presence of montmorillonite and its association with uranium mineralization was inferred from factors 2 and 3 in Table 30. Fig. 71 shows the variation of the factor scores of factor 3, with the carnotite concentration (plotted as U ppm). The mineralized calcrete has a scatter of points about the plotted line, whereas the unmineralized calcretes do not follow the same relationship. It is therefore postulated that crystallization of carnotite was related to the presence of montmorillonite, causing a concretionary-type of uranium accumulation.

The causative factor for the formation of concretions is the heterogeneous nucleation, after dissociation of UDC by soil suction, of uranyl and vanadate molecules by montmorillonite which act as pre-existing seed crystals.

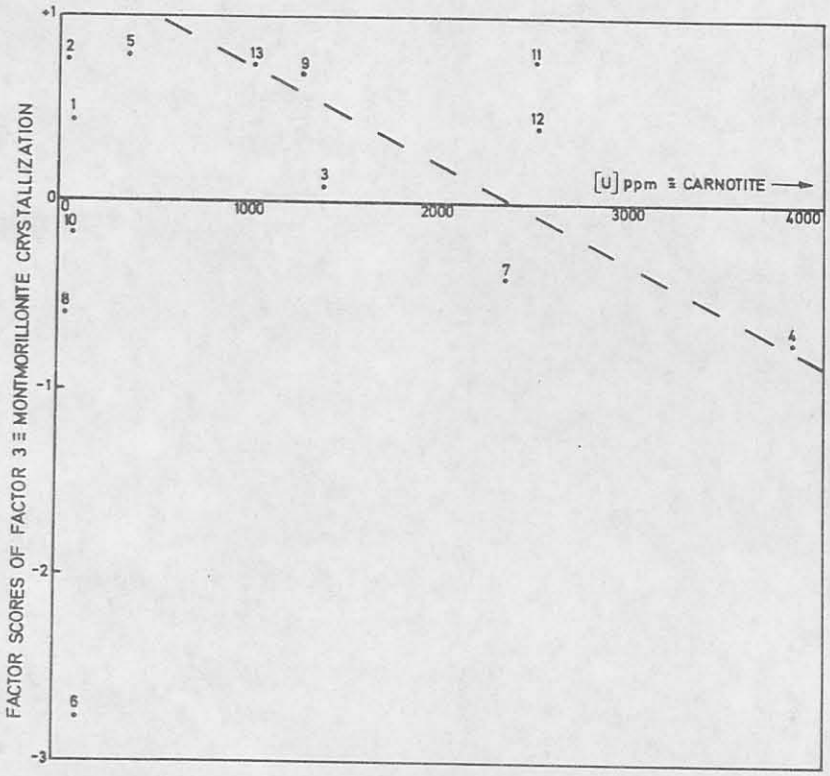

Fig. 71: A plot of the factor scores of factor 3 (Table 34) against carnotite mineralization in terms of the concentration of uranium. (Numbers as in Table 30).

Solids have a certain amount of excess free energy at the surface, which is the main thermodynamic feature of nucleation. Because of the abundance of grain surfaces available on the clay per unit volume of pore solution, heterogeneous nucleation is promoted, and supersaturation (necessary for precipitation) is low, i.e. precipitation from unsaturated solutions is possible (Berner, 1971, p. 95).

Finally there is the question of the differences in age relationship between the initial precipitation of calcite and that of carnotite, which is associated with the rims of the second generation calcite. From the geomorphological point of view the calcrete started to form in the mid-Tertiary.

Carnotite, on the other hand, formed much later.

The origin of the calcium in the calcrete is due to weathering of calcium-bearing minerals. Decomposition of feldspars is fairly rapid and widespread in desert environments. If this was the case for the Langer Heinrich at that period, why was uranium not mobilized and precipitated? The answer to this question must partly remain unsolved, but it can be stated that the activities of uranium, vanadium and potassium only reached their critical values at that time, thereby allowing carnotite to precipitate. Further it is noted that pluvials and interpluvials were characteristic of the Pleistocene (Netterberg, 1969(a)). With the onset of these climatic phases the subsurface water became sufficiently oxidizing and corrosive to leach and transport the uranium from the source rocks to finally precipitate it epigenetically in the calcrete.

14.6 Geochemistry and Origin of Gypcrete

The distribution of the gypcrete is schematically represented in Fig. 2. The main geochemical problem concerning the gypsum is that of its origin.

Martin (1963) proposed that the origin of gypsum was due to the reaction of sulphuric acid, formed from hydrogen sulphide by oxidation, on the calcite in calcrete. The hydrogen sulphide was derived from the gas emanations of the anaerobic basins on the continental shelf. He discounted the possibility of gypsum precipitation from ground-water on the basis that thereaction products would not be continued to

the surface.

It would appear that this interpretation concerning the origin of the gypsum is for the most part unlikely for it is very difficult to conceive that the anaerobic basins would be capable of having produced such large volumes of hydrogen sulphide. A new mechanism is therfore proposed based on sulphate precipitation by onshore fogs. Analyses of seawater and precipitated fog are given in Table 38.

Fog precipitation with the equivalent rainfall in 1958 and the actual mean rainfall at Swakopmund over 35 years is given in Table 39. The interpretation of the results, as calculated from values of both Tables, must be viewed with some caution because of the lapse of the time between the samples in Table 38 and the fog precipitation figures of Table 39. As these are the only figures available, no alternative solution could be found.

TABLE 38: ANALYSES OF SEAWATER AND FOGWATER (COURTESY CSIR)

	Sea= water	Fog 1	Fog 2	Fog 3	Fog 4
pH	7,6	7,3	7,6	7,6	8,1
*Conductivity	43000	13600	1 900	1 240	1 760
+TDS (ppm) (180 °C)	37562	9860	1 290	795	1 175
Na (ppm)	10900	2580	308	213	290
K (ppm)	71	100	11	6	26
SO_4 (ppm)	2683	1158	174	88	221
(NO_3) as N (ppm)	Trace	12,3	7,0	3,4	9,6
(NO_2) as N (ppm)	ND				
SiO_2(ppm)	2	7,5	7,5	7,5	7,5
F (ppm)	0,9	8,8	1,9	0,4	1,7
Cl (ppm)	19690	4598	502	371	412
ΣCO_3 (ppm)	75	63	32	23	67
Ca (ppm)	118	292	49	36	40
Mg (ppm)	1281	217	35	19	46
NH_3 (ppm)	ND	Trace	Trace	Trace	Trace
PO_4 (ppm)	Trace	-	-	-	-
Sr (ppm)	5	-	-	-	-
B (ppm)	5	-	-	-	-

Seawater: Collected September, 1974, from beach between Walvis Bay and Swakopmund.
Fog 1 : Collected July 1966, Walvis Bay
Fog 2 : Collected 4 September, 1966, Rooibank
Fog 3 : Collected 13 August, 1966, Rooibank
Fog 4 : Collected from Gobabeb, analyzed 13 September 1966.

All analyses done by National Institute of Water Research, Windhoek.

Results of Fog 1 to 4 are by courtesy of the Transvaal Museum.

* Conductivity units, mho.

+ TDS = Total dissolved solids.

TABLE 39: FOG PRECIPITATION, EQUIVALENT RAINFALL IN 1958 AND ACTUAL MEAN RAINFALL AT SWAKOPMUND (NAGEL, 1962, p. 57)

MONTH	FOG PRECIPITATION IN 1958 (LITRES)	EQUIVALENT RAINFALL IN 1958 (mm)	ANNUAL MEAN RAINFALL OVER 35 YEARS (mm)
JANUARY	12,0	1,8	1,9
FEBRUARY	14,0	2,2	2,6
MARCH	29,1	4,5	5,3
APRIL	69,0	10,6	1,9
MAY	167,5	25,7	0,7
JUNE	112,0	17,2	0,2
JULY	156,3	24,1	0,3
AUGUST	143,3	22,0	0,7
SEPTEMBER	52,6	8,1	0,7
OCTOBER	27,0	4,2	0,9
NOVEMBER	32,3	5,0	1,0
DECEMBER	30,7	4,7	1,7
TOTAL/YEAR	845,8	130,1	17,9

Within the confines of the anaerobic basins on the continental shelf, the ocean water and the desert stretching to the Langer Heinrich, sulphur follows a definite cycle (Fig. 72). $(H_2S)_B$ is formed in the diatomaceous muds, which contain the sulphate-reducing desulfovibrio bacteria.

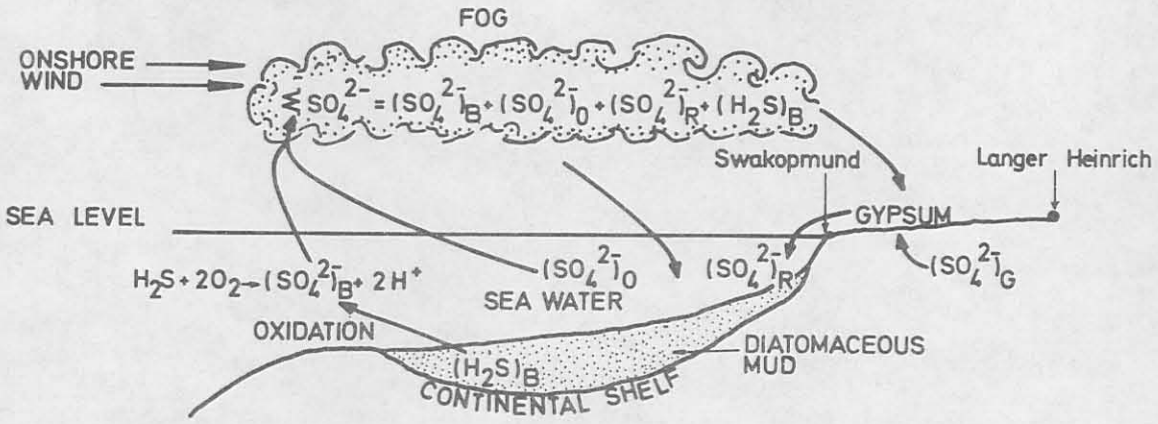

Fig. 72: The sulphur cycle in the diatomaceous sediments of the continental shelf, the Atlantic Ocean and the Namib Desert.

Upon being released to the seawater, having its own initial sulphate content, $(SO_4^{2-})_O$, part of it is oxidized to sulphate $(SO_4^{2-})_B$, thereby contributing in a small measure to the total sulphate content of the sea. The remainder is released to the atmosphere as $(H_2S)_B$. A very small amount of sulphate $(SO_4^{2-})_R$ is contributed by ephemeral drainage such as the Swakop River.

Onshore winds pick up water nuclei from the seawater (not just water from evaporation, as this will not contain significant dissolved solids) causing the formation of fogs which can be blown up to about 100 km inland. The sulphur balance in the fogwater will be made up of the following components:

$$\sum SO_4^{2-} = (SO_4^{2-})_B + (SO_4^{2-})_O + (SO_4^{2-})_R + (H_2S)_B \qquad (14.4)$$

The initial seawater sulphate will more than likely constitute the greater part of the total amount in equation (14.4). Condensation or precipitation of the fogwater in the desert takes place and the sulphate is precipitated as gypsum. A certain amount of sulphate $(SO_4^{2-})_G$ is contributed to this gypsum from the ground-water. A study of the sulphur isotopes within each unit of this system would be the only way in which to confirm or disprove this theory. As this is not currently possible, evaluation of the amount of the sulphate precipitated from the fogs can be calculated from the data in Tables 38 and 39. The months in which the fogs were collected is matched to the fog precipitation, as equivalent rainfall, for the corresponding month. Calcium sulphate precipitated per km^2 per month is tabulated below (Table 40). Assume that by averaging the sulphate contents of the fogs in Table 38, a mean value is obtained. The amount of gypsum (as $CaSO_4$) precipitated per year is calculated as 53 tons per km^2. However rough these estimates may be, they nevertheless serve to show that there is a considerable amount of gypsum that has been, and is being, precipitated anually in the Namib Desert.

A check should be made concerning the relationship of the composition of the fogwater to that of the seawater from which it was derived. For comparison, the composition of the seawater and fogwater are plotted on a Schoeller diagram (Fig. 73) using the technique described by Parker (1969, p. 120).

TABLE 40: PRECIPITATION OF GYPSUM EXPRESSED AS $CaSO_4$ IN TONS/km^2/MONTH

Month	Equivalent rainfall 1958 (mm)	$CaSO_4$ (tons/km^2/month)			
		Fog 1	Fog 2	Fog 3	Fog 4
July	23,1	39,6			
August	22,0			2,7	
September	8,1		2,0		2,6

The plot of the seawater follows the same trend and dimensions as the seawater in other parts of the world (ibid., p. 117). Trends for all the fogwaters follow very similar patterns with the exception of magnesium, which shows only a slight relative depletion with respect to the seawater. This confirms that the fogs were derived from seawater and were taken bodily as nuclei from the surface of the ocean and diluted to some extent by water vapour from evaporation.

14.7 Isotopic Disequilibrium of Uranium

This section deals with the state of equilibrium between the respective uranium isotopes and other daughter products.

Chemical separation procedures for thorium, protac=tinium and uranium are given in Chapter 7. Sources were counted until a maximum standard deviation of 3 per cent was obtained for each peak area.

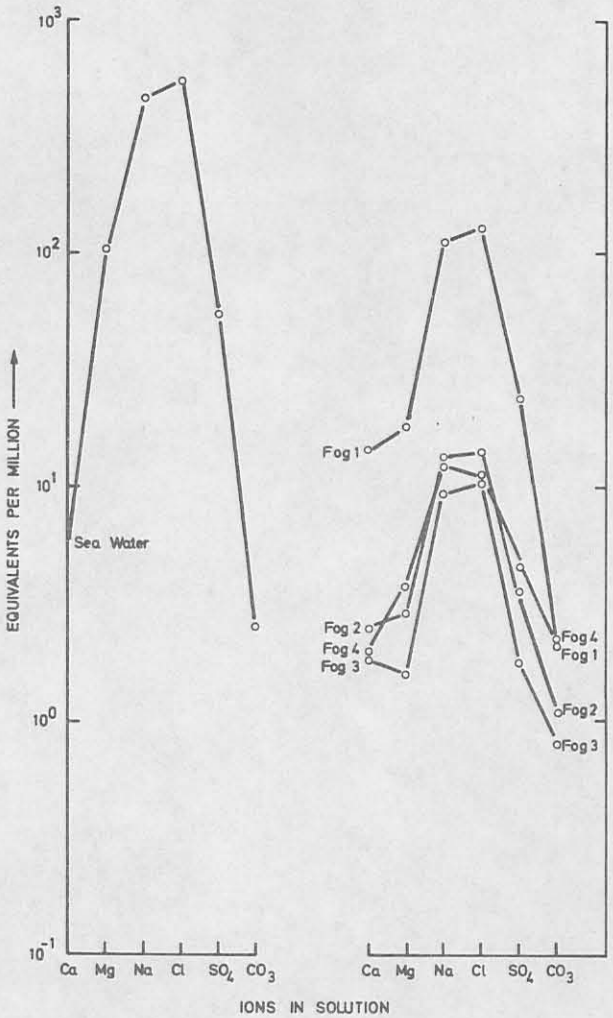

Fig. 73: Schoeller diagram, comparisons of the ionic distributions in sea- and fogwaters in terms of equivalents per million ionic species.

14.7.1 Isotopic equilibrium and disequilibrium

Equilibrium between the isotopes of a particular decay series is reached when all the daughter products decay at the same rate as they are being produced by their respective parents. This means that if equilibrium is to be reached, the activity ratio of the daughter product to that

of its parent must be constant. If this value deviates from the theoretical constant then a condition of disequilibrium has been created.

In the geological environment the equilibrium can be disturbed by some or other event during which uranium is removed from its place of origin and redeposited elsewhere.

Accompanying the decay of ^{238}U, a large amount of energy is released in the form of α-particles having an energy of about 4,2 MeV. From the conservation of momentum, the recoil energy imparted to the nucleus (now ^{234}Th) is simply

$$4{,}2 \left[\frac{\text{Mass of } \alpha\text{-particle}}{\text{Mass of } ^{234}\text{Th nucleus}}\right] \approx 0{,}07 \text{ MeV} \qquad (14.5)$$

The bond energy of most uranium compounds is less than 10 eV, therefore the transformed nucleus escapes from chemical bonding. Two mechanisms based on this concept have been suggested to account for the ^{234}U disequilibrium.

(a) ^{234}U is relocated, after recoil, into crystal defects and microcracks where it becomes more accessible to oxidation and subsequent removal in solution as the uranyl ion (Cherdyntsev et al, 1964).

(b) Rosholt et al (1965, 1966) suggested that as a result of recoil, breaking of chemical bonds takes place, accompanied by stripping of outer electrons by β-decay, thereby converting it in situ to the hexavalent form.

The difference between the two mechanisms is that in the first case the ^{234}U is subjected to selective exposure,

making it more susceptible to oxidation. In the second case the ^{234}U from its inception is in the hexavalent state and therefore does not require the need of external environmental oxidizing conditions.

Kolodny and Kaplan (1970) found in their study of phosphorites that case (a) was the most likely mechanism to account for the disequilibrium in the uranium isotopes.

In Table 41 the $^{234}U/^{238}U$ activity ratio is given for various duricrust samples from the Langer Heinrich and Von Stryk's pit. Equilibrium in most cases has not been completely established, but the deviations from unity are small. Only sample HJ2-13 falls below one. Generally, uranium is still migrating and being deposited with the exception of HJ2-13 where some in situ leaching has taken place.

TABLE 41: $^{234}U/^{238}U$ ACTIVITY RATIOS FOR THE DURICRUSTS OF THE LANGER HEINRICH AND VON STRYK'S PIT

Sample No.	$^{234}U/^{238}U$
HJ2-3	1,05
HJ2-5	1,00
HJ2-8	1,03
HJ2-10	1,03
HJ2-13	0,96
AD1-1	1,01
AD1-4	1,03
AD1-17	1,13
C5-15	1,02
Von Stryk's pit	1,01

The Bloedkoppie Granite has partially contributed to the supply of uranium to the duricrusts. From the $^{234}U/^{238}U$ activity ratio in the granites (Table 42), both precipitation

and leaching of uranium is indicated.

TABLE 42: $^{234}U/^{238}U$ ACTIVITY RATIO FOR THE BLOEDKOPPIE GRANITE

SAMPLE	$^{234}U/^{238}U$
LH16	1,09
HJ2-36	0,86

Sample HJ2-36 was a powder from a percussion borehole, taken from a depth of 27 m and equivalent to 18 m penetration into the granite. Even at this depth uranium is still being leached by subsurface waters. LH16 is an outcrop sample of granite and the high $^{234}U/^{238}U$ activity ratio is indicative of conditions where uranium is still circulating. Some of the uranium in this sample was precipitated after migration from elsewhere.

14.7.2 Geochronology

Disequilibrium has most widely been applied to the field of Pleistocene geochronology (Rosholt, 1970). Two models were developed that described and apply the principles of isotopic fractionation, which are the closed and open systems (Rosholt, 1967; Szabo and Rosholt, 1969).

Nomenclature

$^{230}Th/^{234}U$ = activity ratio of the isotopes ^{230}Th and ^{234}U, etc.

λ_{230} = decay constant for ^{230}Th ($9,2 \times 10^{-6}$)

λ_{231} = decay constant for ^{231}Pa ($2,1 \times 10^{-5}$)

λ_{234} = decay constant for ^{234}U ($2,8 \times 10^{-6}$)

t = time (age of sample, years)

The Closed System

In defining the closed system the assumption is made that all the ^{230}Th is produced by the decay of uranium isotopes that were taken up by the specimen when it was formed. No uranium and thorium were subsequently added or removed from the system. When disequilibrium of ^{234}U is taken into account the age of the samples, t, can be related to the ratio of ^{230}Th activity produced internally to the observed activity of ^{234}U as follows (Szabo and Rosholt, 1969, p. 3254).

$$\frac{^{230}Th}{^{234}U} = \frac{^{238}U}{^{234}U}\left[1-e^{-\lambda_{230}t}\right] + 1,435\left[1-\frac{^{238}U}{^{234}U}\right]\left[1-e^{-\lambda_{230}-\lambda_{234}\ t}\right] \qquad (14.6)$$

The Open System

Isotopic work on shells revealed that more uranium was available to the specimen than was actually assimilated (Rosholt, 1967, p. 299). The ^{231}Pa and ^{230}Th content was contributed by both the assimilated uranium and the mobile uranium which was not retained. An open-system model takes these problems into account and the concepts can be applied in general to the migration and occurrences of uranium in natural material. Fig. 74 represents the migration and decay

of uranium and the paths through which the ^{231}Pa and ^{230}Th accumulated.

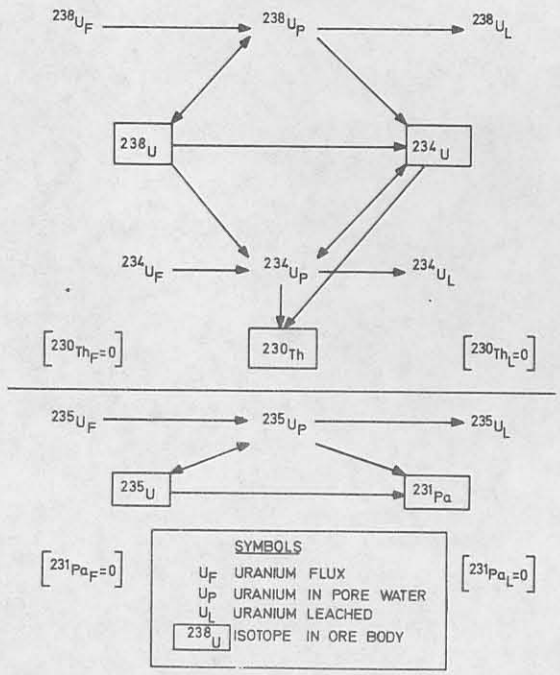

Fig. 74: A flow diagram of uranium and the accumulation of daughter isotopes in an open-system model.

Mathematically the system can be described by the following equations (Szabo and Rosholt, 1969, p. 3255):

$$A = B\left[\frac{k_3 - k_1 k_5}{k_4}\right] + C\left[\frac{k_5}{k_4} - B\,\frac{k_2 k_5}{(k_4)^2}\right] \qquad (14.7)$$

where $A = {}^{230}Th/{}^{234}U$

$B = {}^{231}Pa/{}^{234}U$

$C = {}^{231}Pa/{}^{238}U$

$k_1 = e^{-\lambda_{234}t}$

$k_2 = 1-e^{-\lambda_{234}t}$

$k_3 = 1-e^{-\lambda_{230}t}$

$$k_4 = 1-e^{-\lambda_{231}t}$$

$$k_5 = 1,435\ [1-e^{-\lambda_{230}-\lambda_{234}t}]$$

The open-system model is considered to be superior to the closed-system model as most samples from the natural environment are unlikely to yield to the rigid conditions required by the latter. Furthermore it tries to incorporate a material balance of incoming and outgoing uranium.

Table 43 gives the ages of the uranium mineralization in the calcretes of the Langer Heinrich. The discrepancy between the ages of the closed and open systems clearly indicates that the ore-body was subjected to an open system. Therefore the ore-body has a minimum age of 30 000 years.

TABLE 43: DISEQUILIBRIUM AGES OF URANIUM MINERALIZATION BY CLOSED AND OPEN-SYSTEM MODELS

Sample	$^{230}Th/^{234}U$	$^{231}Pa/^{234}U$	$^{231}Pa/^{238}U$	$^{238}U/^{234}U$	Age (years)	
					Closed	Open
HJ2-10	0,43	-	-	0,97	62000±2000	-
HJ2-13	0.45	0,93	0,96	-	65000±2000	30000±1000

14.7.3 Mass spectrographic analysis

The $^{235}U/^{238}U$ ratio was determined in certain calcrete samples from the Langer Heinrich and one sample of uranothorianite from Phalaborwa, the latter being used as the standard reference (Table 44).

TABLE 44: $^{235}U/^{238}U$ ATOM RATIOS IN CALCRETE FROM THE LANGER HEINRICH AND URANOTHORIANITE FROM PHALABORWA

Sample	$^{235}U/^{238}U$ (Atom %)
HJ2-8	0,007268
HJ2-13	0,007261
AD1-17	0,007247
C5-15	0,007257
Uranothorianite	0,007272

Relative to the uranothorianite, the calcretes are approximately 2 per cent depleted in ^{235}U.

14.8 Summary

Factor analysis of the raw data provided pointers concerning the nature and mechanisms which were involved during the formation of calcrete. Calcite and carnotite were precipitated as independent phases within the pore spaces of the detrital material from mineralized subsurface waters. Limited detail was provided concerning the actual mechanisms involved and therefore the geochemistry of individual and groups of elements was discussed with the possible implications for the development of calcrete duricrust deposits.

Calcite precipitated in the calcrete by the process of soil suction. By analogy, the segregation of carnotite resulted from a transport process, mainly upward diffusion caused by soil suction, and was precipitated by the nucleation of the uranyl ion on montmorillonite.

A new mechanism is proposed for the origin of gypcrete in the Namib Desert, which is based on the precipitation of calcium sulphate from onshore fogs.

The isotope ratio $^{234}U/^{238}U$ for the duricrusts and Bloedkoppie revealed that equilibrium had not been completely established and that the uranium is still migrating. Age determinations of the uranium mineralization using the prin= ciples of isotopic disequilibrium based on the closed-system and open-system models, were 63 000 years and 30 000 years respectively.